Neurobiology of Disease 121 (2019) 187–204

Contents lists available at ScienceDirect

Neurobiology of Disease

journal homepage: www.elsevier.com/locate/ynbdi

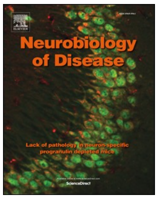

A potential gain-of-function variant of *SLC9A6* leads to endosomal alkalinization and neuronal atrophy associated with Christianson Syndrome

Alina Ilie[a], Andy Y.L. Gao[b], Annie Boucher[a], Jaeok Park[c], Albert M. Berghuis[c], Mariëtte J.V. Hoffer[d], Yvonne Hilhorst-Hofstee[d], R. Anne McKinney[b], John Orlowski[a,*]

[a] *Department of Physiology, McGill University, Montreal, Canada*
[b] *Department of Pharmacology and Therapeutics, McGill University, Montreal, Canada*
[c] *Department of Biochemistry, McGill University, Montreal, Canada*
[d] *Department of Clinical Genetics, Leiden University Medical Center, Leiden, the Netherlands*

ARTICLE INFO

Keywords:
Christianson Syndrome
X-linked intellectual disability
Alkali cation/proton exchangers –SLC9A6/NHE6
Endosomal pH homeostasis
Membrane trafficking
Neurodegeneration

ABSTRACT

Loss-of-function mutations in the recycling endosomal (Na^+,K^+)/H^+ exchanger gene *SLC9A6/NHE6* result in overacidification and dysfunction of endosomal-lysosomal compartments, and cause a neurodevelopmental and degenerative form of X-linked intellectual disability called Christianson Syndrome (CS). However, knowledge of the disease heterogeneity of CS is limited. Here, we describe the clinical features and underlying molecular and cellular mechanisms associated with a CS patient carrying a *de novo* missense variant (p.Gly218Arg; G218R) of a conserved residue in its ion translocation domain that results in a potential gain-of-function. The patient manifested several core symptoms typical of CS, including pronounced cognitive impairment, mutism, epilepsy, ataxia and microcephaly; however, deterioration of motor function often observed after the first decade of life in CS children with total loss of SLC9A6/NHE6 function was not evident. In transfected non-neuronal cells, complex glycosylation and half-life of the G218R were significantly decreased compared to the wild-type transporter. This correlated with elevated ubiquitination and partial proteasomal-mediated proteolysis of G218R. However, a major fraction was delivered to the plasma membrane and endocytic pathways. Compared to wild-type, G218R-containing endosomes were atypically alkaline and showed impaired uptake of recycling endosomal cargo. Moreover, instead of accumulating in recycling endosomes, G218R was redirected to multivesicular bodies/late endosomes and ejected extracellularly in exosomes rather than progressing to lysosomes for degradation. Attenuated acidification and trafficking of G218R-containing endosomes were also observed in transfected hippocampal neurons, and correlated with diminished dendritic branching and density of mature mushroom-shaped spines and increased appearance of filopodia-like protrusions. Collectively, these findings expand our understanding of the genetic diversity of CS and further elucidate a critical role for SLC9A6/NHE6 in fine-tuning recycling endosomal pH and cargo trafficking, processes crucial for the maintenance of neuronal polarity and mature synaptic structures.

Abbreviations: AMPAR, α-amino-3-hydroxy-5-methyl-4-isoxazolepropionic acid receptor; Arf6, ADP-ribosylation factor 6; ARNO, ADP-ribosylation factor nucleotide site opener; AP-1, Chinese hamster ovary (CHO) cells deficient in the Na^+/H^+ exchanger 1 isoform; CANX, calnexin; ChFP, monomeric Cherry fluorescent protein; CNS, central nervous system; CS, Christianson syndrome; DMSO, dimethylsulfoxide; EV, extracellular vesicles; ER, endoplasmic reticulum; ERAD, endoplasmic reticulum-associated degradation; ESCRT, endosomal sorting complex required for transport; FRIA, fluorescence ratiometric image analysis; G218R, mutation of amino acid Gly to Arg at position 218 in NHE6v1; GAPDH, glyceraldehyde-3-phosphate dehydrogenase; GFP, green fluorescent protein; HA, influenza virus hemagglutinin epitope; Hsp70, heat shock protein 70; Lamp1, lysosome-associated membrane protein 1; LE, late endosomes; LeuP, leupeptin/pepstatin; M.I.F, median intensity fluorescence; MVB, multivesicular bodies; OMIM, Online Mendelian Inheritance in Man; PCR, polymerase chain reaction; pHv, vesicular pH; PM, plasma membrane; SDS-PAGE, sodium dodecyl sulfate polyacrylamide gel electrophoresis; SLC9A6/NHE6, (sodium, potassium)/proton exchanger isoform 6; TCL, total cell lysate; Tf, transferrin; TfR, transferrin receptor; TGN, *trans*-Golgi network; TRKB, tropomyosin receptor kinase B; TSG 101, tumor susceptibility gene 101 protein; Ub, ubiquitin; WT, wild-type; XLID, X-linked intellectual disability.

[*] Corresponding author at: Department of Physiology, McGill University, Bellini Life Sciences Bldg., Rm, 166 3649 Promenade Sir-William-Osler, Montreal H3G 0B1, Canada.

E-mail address: john.orlowski@mcgill.ca (J. Orlowski).

https://doi.org/10.1016/j.nbd.2018.10.002
Received 19 July 2018; Received in revised form 18 September 2018; Accepted 3 October 2018
Available online 05 October 2018
0969-9961/

1. Introduction

Christianson Syndrome (CS; OMIM 300243) is a rare but increasingly diagnosed neurodevelopmental and regressive form of X-linked intellectual disability (XLID) first described in a multigenerational South African family in 1999 (Christianson et al., 1999). The causative gene, *SLC9A6* (solute carrier family 9, member A6), was identified at chromosomal position Xq26.3 in 2008 and encodes the (Na^+, K^+)/H^+ exchanger isoform 6 (also called *NHE6*) (Gilfillan et al., 2008). Since then, over 50 different mutations in NHE6 have been identified worldwide, many causing premature truncation of the protein in its N-terminal transmembrane domain that likely results in total loss-of-function (Gilfillan et al., 2008; Pescosolido et al., 2014) (also see supplementary data Tables S1 and S2, and databases ClinVar (https://www.ncbi.nlm.nih.gov/clinvar/) and DECIPHER (https://decipher.sanger.ac.uk/)). The CS population frequency is estimated to range from 1 in 16,000 to 100,000 (Pescosolido et al., 2014), although this may be an underestimate due to incomplete diagnoses. In addition to significant limitations in cognitive abilities and social/behavioral adaptive skills, all affected males lack speech despite noticeable auditory perception, and most have seizures, microcephaly, ataxia, atrophy and neuronal loss in brain regions including the cerebellum and brain stem, and reduced life expectancy. While most female carriers are asymptomatic, they may present with mild learning and behavioral difficulties (Christianson et al., 1999; Masurel-Paulet et al., 2016; Sinajon et al., 2016). Deficits in NHE6 function may also extend to other neurodevelopmental disorders, as significantly reduced NHE6 gene expression has been described in postmortem cerebral cortex from patients with idiopathic autism (Schwede et al., 2013); further suggesting a critical role for this transporter in cognitive development. However, the spectrum and frequency of clinical symptoms and genotype-phenotype correlations remain to be documented.

NHE6 is expressed in most tissues (Fagerberg et al., 2014) but is highest in the central nervous system (CNS), consistent with the prominent neuropathologic phenotype of CS. In non-neuronal cells, it is abundant in recycling endosomes together with the transferrin receptor (TfR) (Brett et al., 2002; Nakamura et al., 2005). Loss of NHE6 function results in excess endosomal acidification, impaired TfR trafficking and dissolution of epithelial apical surface polarity (Ilie et al., 2016; Ohgaki et al., 2010; Xinhan et al., 2011). In the CNS, NHE6 has been extensively studied in mouse hippocampal neurons and found in vesicles throughout the soma, dendrites and dendritic spines (*i.e.*, the postsynaptic compartment) that also contain glutamatergic α-amino-3-hydroxy-5-methyl-4-isoxazolepropionic acid receptors (AMPARs) (Deane et al., 2013) and neurotrophin tropomyosin receptor kinase B (TRKB) (Ouyang et al., 2013). It is also present in ill-defined vesicles along axons and at most presynaptic boutons (Deane et al., 2013; Ouyang et al., 2013) and is linked to neuronal growth, maturation and excitatory synaptic transmission; processes that govern memory and learning. Indeed, loss of NHE6 function in knockout mice results in a CS-like neuropathologic phenotype with reduced hippocampal and cortical pyramidal neurite branching, synapse density, and circuit function (Ouyang et al., 2013) and patterned degeneration of cerebellar Purkinje cells that correlate with dysfunction of the endolysosomal pathway and deficits in mouse visuospatial memory and motor coordination (Sikora et al., 2016; Stromme et al., 2011). However, the molecular and cellular mechanisms responsible for this disorder have yet to be fully defined. Only a few human variants which leave the transporter intact have been studied at the molecular and cellular levels (Ilie et al., 2016; Ilie et al., 2014; Roxrud et al., 2009). Understanding the underlying pathobiology of CS may suggest novel therapeutic strategies for the disease.

Herein we report on a Dutch family in which a male presented with CS-like symptoms. Exome sequencing of the X chromosome of family members identified a *de novo* variant in *NHE6* (Xq26.3:g.135080689G > A:NM_001042537.1:c.652G > A:p.Gly218 Arg) of the affected male that results in substitution of a highly conserved glycine at position 218 with an arginine in the transmembrane domain of the longest splice-variant of NHE6 (*i.e.*, NHE6v1). We investigate the effects of this mutation on the biosynthetic processing, stability and membrane trafficking of NHE6 and its impact on endosomal function and neuronal morphology. These results identify a novel molecular pathology for organellar pH-regulating transporters and provides further insight into the pathogenesis of this important neurological syndrome.

2. Materials and methods

2.1. Antibodies and reagents

Mouse monoclonal anti-hemagglutinin (HA) antibody was purchased from Covance Inc. (Berkeley, CA); rabbit polyclonal anti-HA, mouse monoclonal anti-GAPDH, rabbit polyclonal anti-Lamp1, and rabbit monoclonal anti-TSG101 were obtained from Abcam Inc. (Cambridge, MA); mouse monoclonal anti-Flag M2 antibody was from Sigma; rabbit polyclonal anti-GFP antibody was from Life Technologies. Rabbit polyclonal anti-calnexin and mouse monoclonal anti-Hsp70 antibodies were from Enzo Life Sciences, Inc. Mouse monoclonal anti-ubiquitin antibody (P4D1) was obtained from Santa Cruz Biotechnology. Rabbit polyclonal anti-cleaved caspase-3 (Asp175) (cCASP3) antibody was purchased from Cell Signaling Technology. The mEmerald GFP-tagged TGN46 was a gift from Michael Davidson (Addgene, mEmerald-TGNP-N-10 plasmid # 54279). Rab4-GFP, Rab5-GFP, and Rab7-GFP were a kind gift from Dr. Terry Hébert (McGill University). Horseradish peroxidase-conjugated secondary IgG antibodies were purchased from Jackson ImmunoResearch Laboratories (West Grove, PA). All Alexa Fluor® conjugated secondary antibodies were purchased from Molecular Probes (Eugene, OR). Alpha-minimum essential medium (α-MEM), fetal bovine serum, penicillin/streptomycin, and trypsin-EDTA were purchased from Wisent (Saint-Bruno, QC, Canada). The DMEM/F12 medium was from Corning. All other chemical and reagents were obtained from BioShop Canada (Burlington, ON, Canada), Sigma or Fisher Scientific and were of the highest grade available.

2.2. Genetic analyses

Whole-exome sequencing (WES) was performed using a trio diagnostic approach (proband and both parents). Genomic DNA was extracted from blood and fragmented into 200 to 500 bp fragments by means of Adaptive Focused Acoustics (Covaris Inc., Woburn, USA) shearing according to the manufacturer's protocol. Exome capture was performed by means of SureSelectXT Human all Exon v5 kit (Agilent, Santa Clara, USA) accompanied by Illumina paired-end Sequencing library preparation, sequencing on the Illumina HiSEQ2500 (Illumina, San Diego,USA), generating 2 × 100 bp paired end reads with at least 70× median coverage. The in-house sequence analysis pipeline Modular GATK-Based Variant Calling Pipeline (MAGPIE) (LUMC Sequencing Analysis Support Core, LUMC) based on read alignment using Burrows-Wheeler Alignment (BAM-MEM) (http://arxiv.org/abs/1303.3997) and variant calling using Genome Analysis Toolkit (GATK) (McKenna et al., 2010) was used to map FASTQ files, generate BAM files, mapping and variant calling. Reads were aligned to human genome build GRCh37/UCSC hg19. Variants were annotated using variant effect predictor (VEP, Ensembl) for calling of variants in coding regions and intron boundaries. Using variant databases (dbSNP132, ExAC and the 1000 Genomes Project database), frequent (> 5%) variants were excluded. LOVDplus (Leiden Genome Technology Center, LUMC, Leiden) was used for further analysis of variants. The data generated were deposited in the DECIPHER database (patient 368,102; http://decipher.sanger.ac.uk) (Firth et al., 2009).

2.3. Animal procedures

All procedures for animal handling were approved by the McGill

University Facility Animal Care Committee (FACC) and carried out in full compliance with the Policies and Guidelines of the Canadian Council on Animal Care (CCAC).

2.4. Recombinant DNA constructs and mutagenesis

The long transcript splice-variant of human NHE6 (NHE6v1; NCBI NM_001042537) was cloned from a human brain Matchmaker™ cDNA library (Clontech) using PCR methodology and was engineered to contain the influenza virus hemagglutinin (HA) (YPYDVPDYAS) epitope at its extreme C-terminal end as described previously (Ilie et al., 2014). NHE6$_{HA}$ was then used as a template to engineer the G218R missense mutation by PCR mutagenesis. The same templates was also used to introduce a triple Flag epitope in the first extracellular loop immediately after residue Met53 (Ilie et al., 2014). Enhanced green fluorescent protein (GFP) and monomeric Cherry fluorescent protein (ChFP) were also fused to the C-terminus NHE6 WT and G218R mutant. Insertion of the different epitope tags in the various positions did not alter the biochemical properties or cellular distribution of exogenous NHE6 compared to the endogenous protein (Ilie et al., 2014). All constructs were sequenced to insure that no additional mutations were introduced during PCR.

2.5. Cell culture

Chinese hamster ovary AP-1 and HeLa cells were cultured in α-MEM supplemented with 10% fetal bovine serum, penicillin (100 units/ml), streptomycin (100 μg/ml), and 25 mM $NaHCO_3$ (pH 7.4). Primary cultures of mouse hippocampal neurons were prepared from postnatal day (PD) 0–2 day C57BL/6 mice as described previously (Deane et al., 2013; Ilie et al., 2014).

2.6. Western blotting

For western blot analyses, AP-1 and HeLa cells were grown in 10-cm dishes and transiently transfected with 5 μg of plasmid DNA encoding NHE6$_{HA}$ wild-type or mutant constructs using Lipofectamine2000™ (Invitrogen), as described previously (Ilie et al., 2016).

2.7. Cell surface biotinylation

Extraction of biotinylated plasma membrane proteins was performed by treating cells with the membrane-impermeable reagent N-hydroxysulfosuccinimydyl-SS-biotin (0.5 mg/ml) (ThermoScientific, Rockford, IL) as previously described (Ilie et al., 2016).

2.8. Isolation of extracellular membrane vesicles

AP-1 cells were grown in 15-cm dishes (5 for each construct) and transfected with 20 μg of NHE6$_{HA}$ WT or G218R in serum-free α-MEM using Lipofectamine2000. Twenty-four hours after transfection, the culture medium was collected in 50-ml Falcon tubes and centrifuged at 500 ×*g* for 5 min, then at 2000 ×*g* for 10 min, in order to remove any intact cells and cell debris. The supernatant resulting from these two centrifugations was concentrated to 1.5 ml using Amicon® Ultra-15 centrifugal filters with 100,000 NMWL (Nominal Molecular Weight Limit), according to the manufacturer's instructions. This concentrated culture medium was subjected to ultracentrifugation at 100,000 ×*g* for 2 h at 4 °C to obtain the membrane fraction. The resulting pellet was washed in 1.5 ml PBS and re-centrifuged at 100,000 ×*g* for 1.5 h at 4 °C. The membrane vesicle-enriched pellet was resuspended in lysis buffer and stored at −80 °C. Total cellular lysates were also obtained by lysing the cells of each dish in 1.5 ml lysis buffer. Protein concentrations were measured and 40 μg of exosomal protein, along with 10 μg of total cellular protein, were subjected to SDS-PAGE and immunoblotting with the indicated antibodies. On average, the total protein levels of the exosomal preparations for WT- and G218R-transfectants represented ~3–4% of the total cell lysate protein content.

For chloroquine treatment, AP-1 cells were transfected with NHE6$_{HA}$ WT or G218R in serum-free α-MEM for 10 h, then the medium was changed to serum-free α-MEM containing no chloroquine (control samples) or 250 μM chloroquine for 15 h. Extracellular vesicles and total cellular lysates were then obtained as described.

2.9. Neuronal DNA transfection

Primary hippocampal neuronal cultures were prepared from C57BL/6 mice and co-transfected at 10–12 days *in vitro* (DIV) with GFP and mCherry fluorescent protein (ChFP) or NHE6$_{ChFP}$ WT or G218R by calcium phosphate-mediated transfection as previously described (Ilie et al., 2016).

2.10. Immunofluorescence confocal microscopy

AP-1 cells were cultured on fibronectin-coated 18-mm glass coverslips, transfected with $_{3F}$NHE6$_{HA}$ WT or G218R mutant, and fixed 24 h post-transfection with 4% paraformaldehyde for 20 min at room temperature. To label NHE6 present on the plasma membrane, cells were incubated with mouse monoclonal anti-Flag antibody (1:1000) in PBS-CM/10 mM glucose/10 mM HEPES/2% goat serum, pH 7.4 for 1 h at room temperature (wash buffer), washed 4 times, and then incubated with goat anti-mouse Alexa Fluor® 488-conjugated secondary antibody (1:1300) for 1 h at room temperature. After extensive washes with PBS, cells were permeabilized with 0.1% saponin/PBS for 20 min at room temperature and then incubated with rabbit polyclonal anti-HA antibody (1:400) in wash buffer supplemented with 0.01% saponin at 4 °C overnight to label the total cellular pool of NHE6. After washes with PBS, cells were labelled with goat anti-rabbit Alexa Fluor® 568-conjugated secondary antibody (1:1200) for 1 h at room temperature, washed, and mounted onto glass slides.

To examine the subcellular distribution of WT and G218R mutant, AP-1 cells were co-transfected with NHE6$_{ChFP}$ WT or G218R and different GFP-tagged organellar markers (Rab4, Rab5, Rab7, and TGN46), fixed and mounted 24 h post-transfection. To label transferrin-containing recycling endosomes, AP-1 cells transfected with NHE6$_{ChFP}$ WT or G218R for 24 h, were incubated with Alexa Fluor® 488-conjugated transferrin (Tf-AF^{488}) for 45 min in serum-free α-MEM, washed, fixed, and mounted. To visualize the ER and lysosomes, AP-1 cells expressing NHE6$_{ChFP}$ WT or G218R were fixed 24 h after transfection and labelled with rabbit polyclonal anti-calnexin or anti-Lamp1 primary antibodies, respectively, followed by goat anti-rabbit Alexa Fluor® 488-conjugated secondary antibodies, washed, and mounted. Cells were examined by laser scanning confocal microscopy using the ZEN software of a Zeiss LSM 780 microscope equipped with a PMT detector, with images acquired using a 63 ×/1.4 NA oil immersion objective lens.

Mounted primary hippocampal cultures were imaged using a Leica SP2 confocal microscope. Images were acquired using 40× and 63× HCXPL APO oil-immersion objectives (NAs 1.25 and 1.4, respectively). GFP was imaged using a 488 nm Ar laser line; mCherry was imaged using a 543 nm HeNe laser line, and DyLight 649 was imaged using the 633 nm HeNe laser line. Channels were acquired sequentially to prevent spectral overlap of fluorophores. Optical sections of 300–500 nm were taken and frame averaged 3× at low resolution or line-averaged 2× at high resolution to improve the signal-to-noise ratio. Images were first deconvolved using Huygen's Essential software by using a full maximum likelihood extrapolation algorithm (Scientific Volume Imaging), and 3D images were compiled as maximum intensity projections using Imaris software (Bitplane Ag).

Topographical order of neuronal morphology was performed on 3D confocal images of primary hippocampal neurons prepared from C57BL/6 mice. Images were analyzed using the FilamentTracer program (Bitplane AG, Zurich, Switzerland), which semi-automatically detects 3D neuronal GFP-labelled filament structures and calculates parameters such as the number of branch points, total dendrite length and area.

2.11. Measurement of endosomal pH

AP-1 cells for grown overnight on FluoroDishes™ (World Precision Instruments, Inc.) coated with fibronectin/PBS (2 µg/ml, for 2–4 h at 37 °C). Cells were transfected with 1 µg/dish of NHE6v1 (WT or G218R) containing pHluorin2 in the first extracellular loop (inserted at amino acid position M53) ($_{\mathrm{pH2}}$NHE6v1) using Lipofectamine2000 reagent according to the manufacturer's instructions. Twenty-four h after transfection, cells were incubated for 5 h with 100 µg/ml cycloheximide in complete medium. Before imaging, cells were switched to CO_2-independent medium. Vesicular pH was measured by single-cell fluorescence ratiometric imaging analysis (FRIA) at 37 °C, using a Zeiss LSM 780 confocal microscope, equipped with a PMT detector. Images were acquired with a 63 × /1.4 NA oil immersion objective lens by sequential line scanning at 405 and 488 excitation wavelengths, with emission set at 500–550 for both channels. All cells were imaged in a heated chamber (37 °C) at 3 × zoom, while the laser power, resolution, speed of scanning, digital gain and offset, pinhole opening and line averaging were identical for both channels. Average intensities of fluorescent puncta (0.3 to 3 µm in diameter) were obtained for both the 405 and 488 channels using the MetaXpress software (Molecular Devices, Downingtown, PA) and 488/405 ratios were calculated. Calibration curves of fluorescence as a function of vesicular pH were performed *in situ* in AP-1 cells expressing $_{\mathrm{pH2}}$NHE6v1 WT by clamping the vesicular pH between 5 and 7.8 in K^+-rich medium (135 mM KCl, 10 mM NaCl, 20 mM Hepes or 20 mM MES, 1 mM $MgCl_2$, and 0.1 mM $CaCl_2$) with 10 µM nigericin, 10 µM monensin, 0.4 µM bafilomycin and 20 µM carbonyl cyanide *m*-chlorophenyl hydrazone (CCCP) and recording the 488/405 fluorescence ratios, as described above. The calibration curves and Gaussian distributions of vesicular pH values were plotted with OriginPro 8 software (OriginLab, Northampton, MA).

2.12. Flow cytometry

To measure transferrin uptake by flow cytometry, HeLa cells were transfected with GFP alone, NHE6$_{\mathrm{GFP}}$ WT or G218R mutant using FuGene6 (Promega). Twenty-four h after transfection, the cells were serum-depleted for 2 h, and then incubated with Alexa Fluor® 633-conjugated transferrin (Tf-AF^{633}, 10 µg/ml) for 5 min at 37 °C, followed by washes to remove unbound transferrin. Cells were detached from the plates by trypsinization and 5 µl of the cell viability dye 7-amino-actinomycin D (7-AAD, eBioscience) was added to each cell suspension. Cells were analyzed by flow cytometry using a FACS Aria Sorter (Becton Dickinson, San Jose, CA). A gate was set around the GFP-positive cells and the amount of Tf-AF^{633} taken up by 10^4 GFP-expressing live cells (*i.e.*, 7-AAD negative) was measured using the BD FACS Diva software.

2.13. Statistical analyses

The data represent the mean ± the standard error of the mean (S.E.) and statistical analyses were performed by using the Student's *t*-test or a one-way analysis of variance (ANOVA) followed by suitable post-hoc tests as indicated (Tukey, Bonferroni, or Dunns). A minimum *p*-value of < 0.05 was considered significant.

3. Results

3.1. Clinical features

The affected male patient, now 22 years of age, was the second child born to non-consanguineous healthy parents of Dutch origin. He also has a healthy older sister (24 years old). The proband displayed many core symptoms ascribed to CS, including severe intellectual disability, epilepsy, absence of verbal communication, happy demeanor, microcephaly, slender physique, truncal ataxia and hyperactivity. Several common secondary symptoms were also evident, including autism-like behaviors, ophthalmoplegia, flexed arms, sleep disturbances, low weight, excessive drooling and incontinence; however, motor regression that often manifests after the first decade of life in CS children with complete NHE6 loss-of-function was not apparent. A more complete clinical description and list of symptoms compared to a subset of other CS families (where comparable clinical information was available) is presented in supplementary Table S1.

3.2. Mutation analyses

Extensive genetic analyses were performed, including single nucleotide polymorphism (SNP)-array analysis, methylation analysis of the Angelman/Prader-Willi region, sequencing of the *UBE3A*- and *SLC6A8*-gene, all without abnormalities. Trio-based whole-exome sequencing revealed two hemizygous missense variants, one in *FGD1* (FYVE, RhoGEF and PH domain-containing protein 1) (Xp11.22:g.54492214A > G:NM_004463.2:c.1412 T > C:p.Val471 Ala) and one in *SLC9A6/NHE6* (Xq26.3:g.135080689G > A:NM_001042537.1:c.652G > A:p.Gly218Arg). The *FGD1* variant was present in the mother, while the sister was not tested for this variant. Mutations in *FGD1* are linked to Aarskog-Scott syndrome (OMIM 300546), also known as faciogenital dysplasia, but the proband did not exhibit clinical features characteristic of this disorder, suggesting the variant is benign. By contrast, the *NHE6* variant was not present in the mother or sister, indicating it was unique to the proband and arose by *de novo* mutation (Fig. 1A). This Gly residue is in the predicted 5th membrane-spanning segment (M5) of NHE6 and is conserved in all human NHE paralogs (Fig. 1B) and NHE6 orthologs from mammals to fruit flies (Supplementary Fig. S1), and hence likely essential for function. Human *NHE6* undergoes alternate splicing at its 5′ untranslated sequence and coding region to generate at least four distinct cytoplasmic mRNAs (NHE6v1 to v4), of which NHE6v1 (701 amino acids, NCBI NM_001042537.1) encodes the longest transcript. The mutation that would be present in all splice variants. The relative abundances and functional differences, if any, between the splice variants are unknown. A list of other documented NHE6 variants (missense, frameshift, nonsense, in-frame deletions, and splice-site variants) linked to Christianson Syndrome are tabulated in supplementary Table S2.

3.3. Structural homology modelling of NHE6

To gain insight into the possible significance of Gly218 for structure and function, we performed homology modelling of *homo sapien* NHE6v1 (*Hs*NHE6v1) using the high-resolution crystal structures of distantly-related bacterial Na^+/H^+ antiporters (15–20% identity; 27–29% similarity), an approach that has been instructive in validating the tertiary conformation of *Hs*NHE1 (Landau et al., 2007; Nygaard et al., 2011). Swiss-Model software was used to generate a 3D structural model of the N-terminal transmembrane region (encompassing residues 74–540) of *Hs*NHE6v1. Its sequence was threaded onto the outward-facing conformation of the *Thermus thermophilus* NapA (*Tt*NapA) structure (Protein Data Bank accession code 5bz3.1.A; 2.30 Å, 15% identity, 27% similarity) (Coincon et al., 2016), which provided the broadest coverage, highest resolution, and best spatial fit among crystallized bacterial Na^+/H^+ antiporters. An alignment of the two sequences is presented in Supplementary Fig. S2A and the resulting theoretical 3D structure of monomeric *Hs*NHE6v1 (*N.B.*, mammalian and bacterial Na^+/H^+ exchangers/antiporters assemble as homodimers) is shown in Fig. 1C. In this model, the alpha carbon atoms of Gly218 and Arg457 are separated by ~5 Å (Fig. 1D). Conservation of these closely packed residues in all mammalian NHEs (Supplementary Fig. S2B) and bacterial antiporters *Tt*NapA (Gly94 and Lys305) and *Ec*NhaA (Gly104

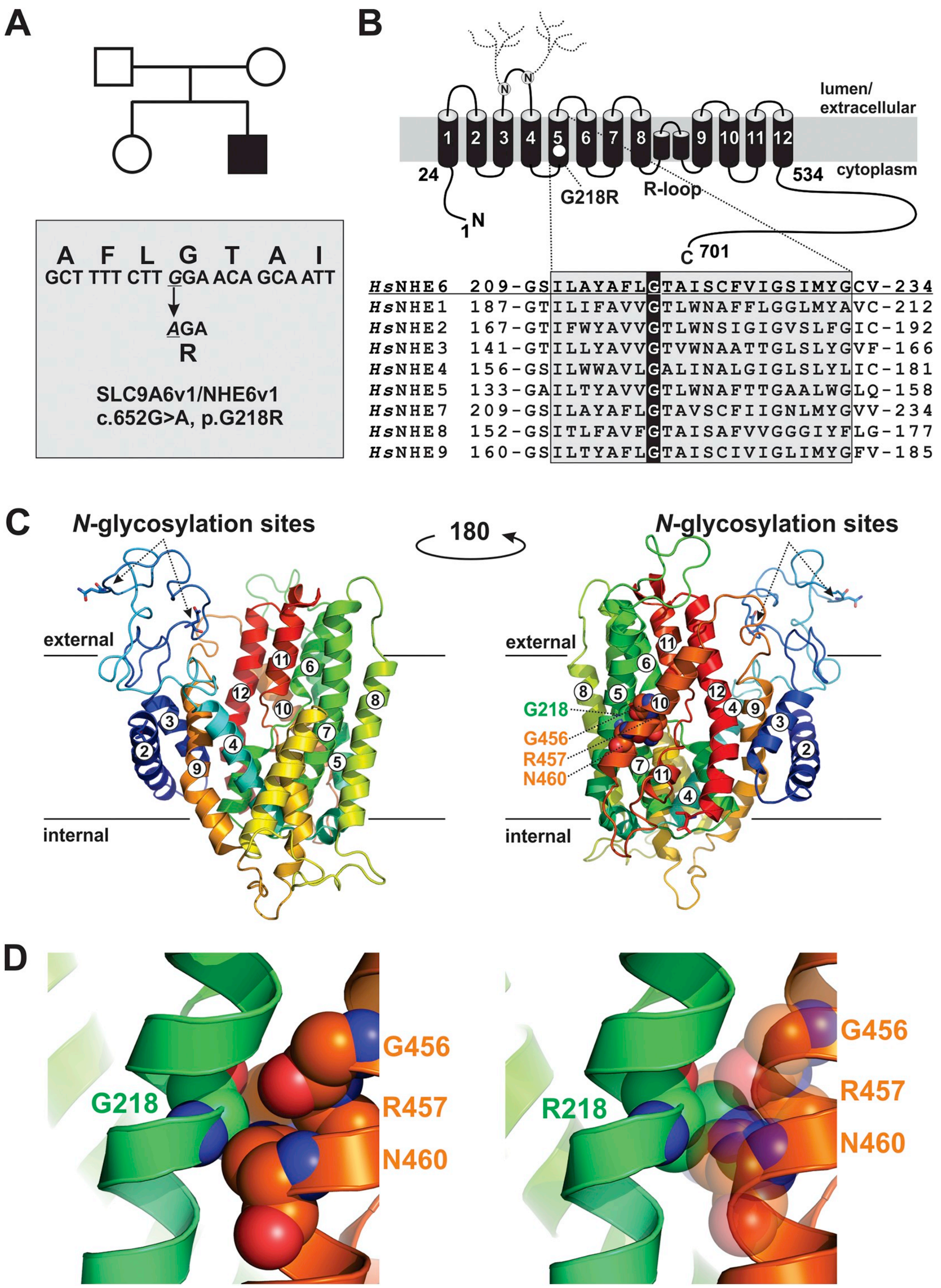

Fig. 1. Identification of a *de novo* missense mutation in SLC9A6/NHE6 in a patient with Christianson Syndrome. *A*, Family pedigree and description of a *de novo* missense mutation (c.652G > A: p.Gly218Arg) (G218R) in the longest splice variant (v1) of SLC9A6/NHE6. B, Schematic planar drawing of the predicted membrane topology of mammalian NHE6v1 based on comparisons of the proposed transmembrane topology of NHE1 (Landau et al., 2007; Nygaard et al., 2011) and location of the pG218R mutation (*white circle*) in the predicted fifth membrane-spanning (M5) helix. Two consensus *N*-glycosylation sites (N128 and N145) within extracellular loop 2 have been verified experimentally (*data not shown*) and are illustrated in the drawing. Also presented is the sequence alignment of the M5 helix and conserved Gly residue of all *Homo sapien* Na$^+$/H$^+$ exchangers (*Hs*NHE1–9). C, Side-view (*left panel*) of a 3D structure homology model of monomeric *Hs*NHE6v1 (*N.B.*, NHEs normally assemble as homodimers) based on the crystal structure of the smaller bacterial *Thermus thermophilus* Na$^+$/H$^+$ antiporter NapA (*Tt*NapA) (Protein Data Bank accession code 5bz3.1.A; 2.30 Å, 15% identity, 27% similarity) (Coincon et al., 2016) which provided the broadest coverage, highest resolution, and best spatial fit compared to other crystallized bacterial Na$^+$/H$^+$ antiporters. The proposed structure includes only the membrane-spanning helices (M2-M12) that aligned with homologous segments of *Tt*NapA as well as the connecting loops and location of the two *N*-glycosylation sites. The opposite side-view (*right panel*) is illustrated to expose the Gly218 residue and neighboring amino acids Gly456, Arg457 and Asn460. D, Enlargement of the region encompassing Gly218 (*left panel*) and analogous representation of the same region where Gly218 and been replaced with Arg218.

and Lys300) suggests they have a critical role. Mutating Arg425 of *Hs*NHE1 (equivalent to Arg457 of *Hs*NHE6v1) markedly reduces its glycosylation, stability, plasma membrane targeting and catalytic activity (Li et al., 2014; Nygaard et al., 2011). Likewise, mutations of Lys305 in *Tt*NapA (Lee et al., 2013) and Lys300 in *Ec*NhaA (Kozachkov et al., 2007; Maes et al., 2012) were found to decrease the substrate affinities and structural integrity of those antiporters (Calinescu et al., 2017). Although the significance of the apposed Gly residue has not been examined, based on homology modelling we speculated that replacement of Gly with a large, positively-charged Arg residue (G218R) would cause steric and electrostatic repulsion between Arg218 and Arg457 (Fig. 1D) and alter the structural stability and catalytic activity of the transporter.

3.4. *Post-translational processing and stability of NHE6-G218R are impaired*

The Chinese hamster ovary-derived AP-1 cell line is a useful expression system for studying and comparing the molecular and cellular properties of NHE6 variants because endogenous NHE6 levels are negligible and its subcellular distribution and behaviour are similar to that in primary and organotypic cultures of hippocampal pyramidal neurons (Deane et al., 2013; Ilie et al., 2016). Immunoblotting for C-terminal HA epitope-tagged NHE6v1 (NHE6v1$_{\mathrm{HA}}$) revealed striking differences between the wild-type (WT) and mutant G218R constructs with respect to their biosynthetic maturation and stability (Fig. 2A). Under SDS-PAGE conditions, NHE6v1$_{\mathrm{HA}}$ migrates as multiple bands reflecting different oligomeric and post-translational oligosaccharide states, consistent with earlier findings (Ilie et al., 2014; Miyazaki et al., 2001). The WT migrates as fully-glycosylated dimeric (~200-.

250 kDa) and monomeric (100–120 kDa) forms, and newly synthesized core-glycosylated (~70 kDa) monomer was also observed. By contrast, G218R migrated predominantly as immature core-glycosylated monomeric and dimeric forms, although a diffuse band corresponding to the fully-glycosylated dimer was also detected suggestive of limited posttranslational processing. Quantitation of the immunoblot signals revealed that total expression of the G218 was significantly reduced compared WT (Fig. 2B).

To estimate the half-lives of WT and G218R, pulse-chase experiments were performed 24 h after transfection. Cells were treated with cycloheximide for an additional 2–24 h to inhibit *de novo* protein synthesis and the levels of the previously synthesized transporters were monitored by immunoblotting. As shown in Fig. 2C-D, WT was relatively stable with a half-life ($t_{1/2}$) exceeding 24 h whereas the G218R mutant was rapidly removed ($t_{1/2}$ of ~1.5 h).

Rapid clearance of the G218R mutant could occur by multiple mechanisms, including proteasomal degradation *via* the ERAD (endoplasmic reticulum-associated degradation) pathway (Meusser et al., 2005) or later in lysosomes by the peripheral quality control ESCRT (endosomal sorting complex required for transport)–dependent degradative pathway (Raiborg and Stenmark, 2009). To explore these possibilities, we first examined G218R ubiquitination (*i.e.*, multi-mono- or poly-ubiquitination), a distinguishing feature of both mechanisms. To compare the ubiquitination of WT and G218R transporters (ub-WT and ub-G218R), they were transiently expressed in AP-1 cells for 24 h, immunoprecipitated from cell lysates, and immunoblots were probed with a monoclonal anti-ubiquitin antibody. The signals for ub-WT and ub-G218R ranged from ~150 kDa to > 250 kDa, which presumably represent ubiquitin conjugates of NHE6 monomers and/or undissociated dimers (Fig. 2E). Ubiquitination of G218R was significantly elevated (~5-fold) compared to WT when normalized to total NHE6 levels in their respective immunoprecipitates (Fig. 2E-F). This also revealed that only minor fractions of total WT and G218R were ubiquitinated.

To identify pathways mediating the degradation of G218R, we exposed cycloheximide-treated cells to inhibitors of proteasomal (MG132, lactacystin) or lysosomal (leupeptin plus pepstatin (LeuP), chloroquine) proteolysis. As expected, the proteasomal and lysosomal inhibitors did not affect WT levels appreciably over 8 h compared to vehicle-treated controls (Fig. 3A). By comparison, inhibiting

the proteasome partially reduced the cellular loss of G218R (Fig. 3B), implicating a limited role for the ERAD pathway. Curiously, the lysosomal protease inhibitors LeuP were ineffective whereas chloroquine was a potent blocker. Unlike LeuP which are direct competitive inhibitors of lysosomal peptidases, chloroquine is a weak base that accumulates in acidic organelles where it becomes protonated (Maxfield, 1982). The resulting alkalinization of these compartments impairs the activities of acidic hydrolases (Seglen et al., 1979). However, given the ineffectiveness of LeuP, and the ability of chloroquine to block the rapid disappearance of G218R suggested it acted through a different mechanism. We postulated that one such pathway could involve exosomes, small lipid vesicles formed by the inward budding of late endosomes (LE) (also termed multivesicular bodies, MVB) (Colombo et al., 2014). When MVB/LE fuse with the plasma membrane rather than with lysosomes, they discharge their intraluminal vesicles (comprised of lipids, proteins and ribonucleic acids) into the extracellular milieu. Similar to the sorting of cargo to lysosomes, ubiquitination (Buschow et al., 2005) and the ESCRT machinery (Colombo et al., 2013) are also involved in the biogenesis and secretion of exosomes.

3.5. *Extracellular vesicular release of G218R*

To assess this possible mechanism, an extracellular vesicular (EV) fraction was prepared using serum-free culture media collected from AP-1 cell cultures transiently expressing either WT or G218R after 24 h using an established differential ultracentrifugation protocol (Greening et al., 2015). High-molecular weight G218R (presumably ub-G218R) was greatly enriched in the EV fraction compared to WT (Fig. 3C). The nature of the EV membrane fraction was confirmed by probing the immunoblots for EV markers, tumor susceptibility gene 101 protein (TSG101, a component of the ESCRT-I complex that recognizes ubiquitinated proteins), and heat shock protein 70 (HSP70, HSPA1A/B, a molecular chaperone that promotes protein folding and also disposal of defective proteins). TSG101 is specific for MVB/LE-derived exosomes whereas HSP70 is in both exosomes and PM-derived microvesicles (also called ectosomes) (Kowal et al., 2016). The levels of both EV markers prepared from WT- and G218R-transfected cells were relatively equivalent, suggesting that expression of G218R did not markedly perturb the net secretion of EVs, but was selectively enriched in them. This was supported by measurements of the absolute protein content of the EV and total cell lysate fractions derived from WT- and G218R-transfected cells. In both cases, the EV fractions were equivalent when expressed as a percentage of the total cell lysates (WT: 3.71% ± 0.19; G218R: 3.70% ± 0.46) (Fig. 3E). As a negative control, immunoblots were also probed for calnexin (CANX), an integral membrane protein involved in endoplasmic reticulum (ER) quality control (Bergeron et al., 1994). As expected, it was virtually absent in the EV fraction (Fig. 3C), which excludes cell lysis as a contributing factor to the extracellular membrane fraction.

Exposure to chloroquine (250 μM, 15 h) blocked secretion of both WT and G218R in EVs and, conversely, increased the total amount of WT and G218R within cells (Fig. 3D). Chloroquine treatment also impaired the oligosaccharide maturation of both constructs, though this was more pronounced for WT. Golgi alkalinization is known to reduce glycosylation (Maeda and Kinoshita, 2010). However, this treatment did not affect the relative levels of either TSG101 or HSP70 in EVs or total cell lysates, indicating that the molecular composition and formation of EVs were not adversely affected by chloroquine. Indeed, chloroquine actually increased the net release of EVs per cell by ~3-fold, although there was no difference between WT and G218R-transfected cells (WT: 11.77% ± 0.59; G218R: 10.24% ± 0.74) (Fig. 3E). Thus, chloroquine may disrupt an earlier pH-dependent step in the trafficking and/or fusion of NHE6-containing endosomes to MVB/LE.

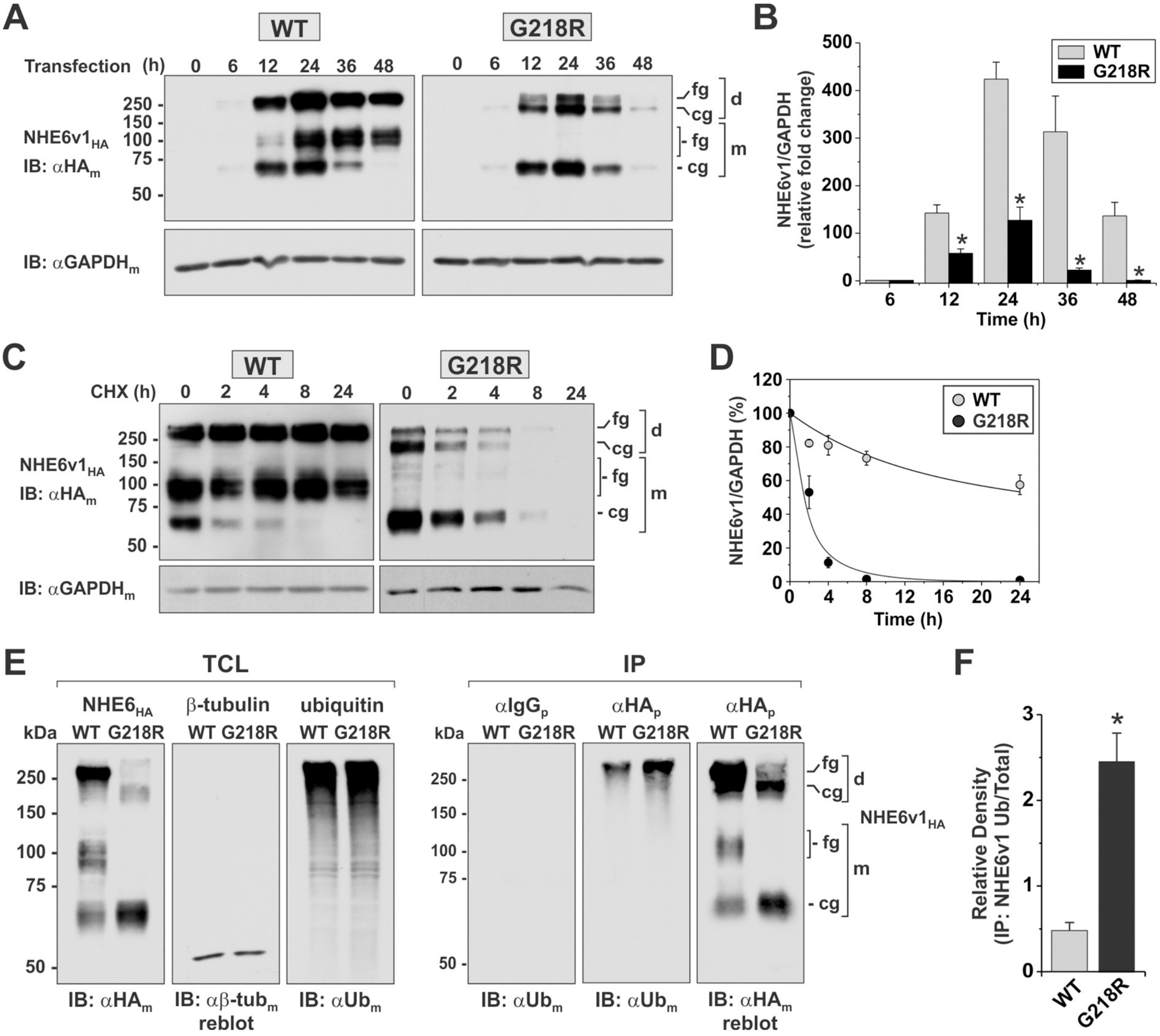

Fig. 2. Biosynthetic maturation and stability of NHE6 is reduced for the G218R mutant. A, AP-1 cells were transiently transfected with NHE6v1$_{HA}$ WT or G218R and lysed at the indicated time points over a 48 h period. Equal amounts of proteins (20 μg) were subjected to Western blotting and probed with a monoclonal anti-HA antibody (αHA$_m$). NHE6v1 migrates as multiple bands: slower migrating high molecular weight bands representing the fully-glycosylated (*fg*) and core-glycosylated (*cg*) dimeric forms of the exchanger (~200 and 175 kDa, respectively) that do not fully dissociate under SDS-PAGE conditions and faster migrating fully-glycosylated (*fg*, ~100 kDa) and core-glycosylated (*cg*, ~70 kDa) forms of the monomeric protein. To control for protein loading, the blots were reprobed with a mouse monoclonal anti-GAPDH antibody (αGAPDH$_m$). B, Densitometric quantification of the relative total cellular abundances of WT, G218R and GAPDH was expressed as a ratio NHE6v1/GAPDH. Data are shown as mean ± standard error of the mean (S.E.) of three different experiments. Statistical significance was assessed using a paired Student's *t*-test, * $p < 0.01$. C, AP-1 cells were transiently transfected with WT or G218R for 24 h and then treated with 150 μg/ml cycloheximide for the indicated time points, lysed and equal amounts of protein (20 μg) were analyzed by Western blotting using a mouse monoclonal anti-HA (αHA$_m$) antibody. Blots were reprobed with a mouse monoclonal anti-GAPDH antibody (αGAPDH$_m$) to control for loading. D, Densitometric quantification of WT and G218R protein abundance (normalized to GAPDH levels) as a function of time in the presence of cycloheximide. Values represent the mean ± S.E. (n = 3). E, AP-1 cells were transiently transfected with NHE6v1$_{HA}$ WT or G218R for 24 h, then lysed and their expression in total cell lysates (TCL) was analyzed by Western blotting with a mouse monoclonal anti-HA (αHA$_m$) antibody (*panel 1*). The blots was stripped and reprobed with a monoclonal antibody to β-tubulin (αβ-tub$_m$) as a loading control (*panel 2*). The level of ubiquitinated proteins in the TCL was examined using a mouse monoclonal anti-ubiquitin (αUb$_m$) antibody (*panel 3*). The TCLs were further subjected to immunoprecipitation (IP) with a non-specific rabbit polyclonal IgG (αIgG$_p$) antibody (*panel 4*) or a rabbit polyclonal anti-HA (αHA$_p$) antibody (*panel 5*) and analyzed with a mouse monoclonal αUb$_m$ antibody to detect ubiquitination of WT and G218R. The membrane from *panel 5* was then stripped and reprobed with a mouse monoclonal αHA$_m$ antibody to examine the total amount of WT and G218R retrieved by immunoprecipitation (*panel 6*). F, Densitometric quantification of the ratio of ubiquitinated to total protein abundance of WT and G218R in the immunopreciptated pellets. Values represent the mean ± S.E. (n = 4). Statistical significance was assessed using a Student's *t*-test, *$p < 0.01$.

ER-resident CANX was not detected in EVs in the absence or presence of chloroquine. However, total cellular levels of CANX were increased upon chloroquine treatment, perhaps due to ER stress (Ruddock and Molinari, 2006).

3.6. G218R causes intracellular mislocalization of NHE6

To gain more insight into the membrane trafficking fate of G218R, we performed subcellular localization analyses using other biochemical and imaging approaches. Most NHE6 WT normally resides in recycling endosomes, however in some cell types a small fraction (~5%) appears on the cell surface through endosomal recycling (Brett et al., 2002), and this was confirmed for AP-1 cells (Supplementary Fig. S3). To determine if the G218R mutant can also traffic to the cell surface, PM localization was assayed using cell surface biotinylation (Le Bivic et al., 1989). Total cellular expression of G218R was ~22% that of WT

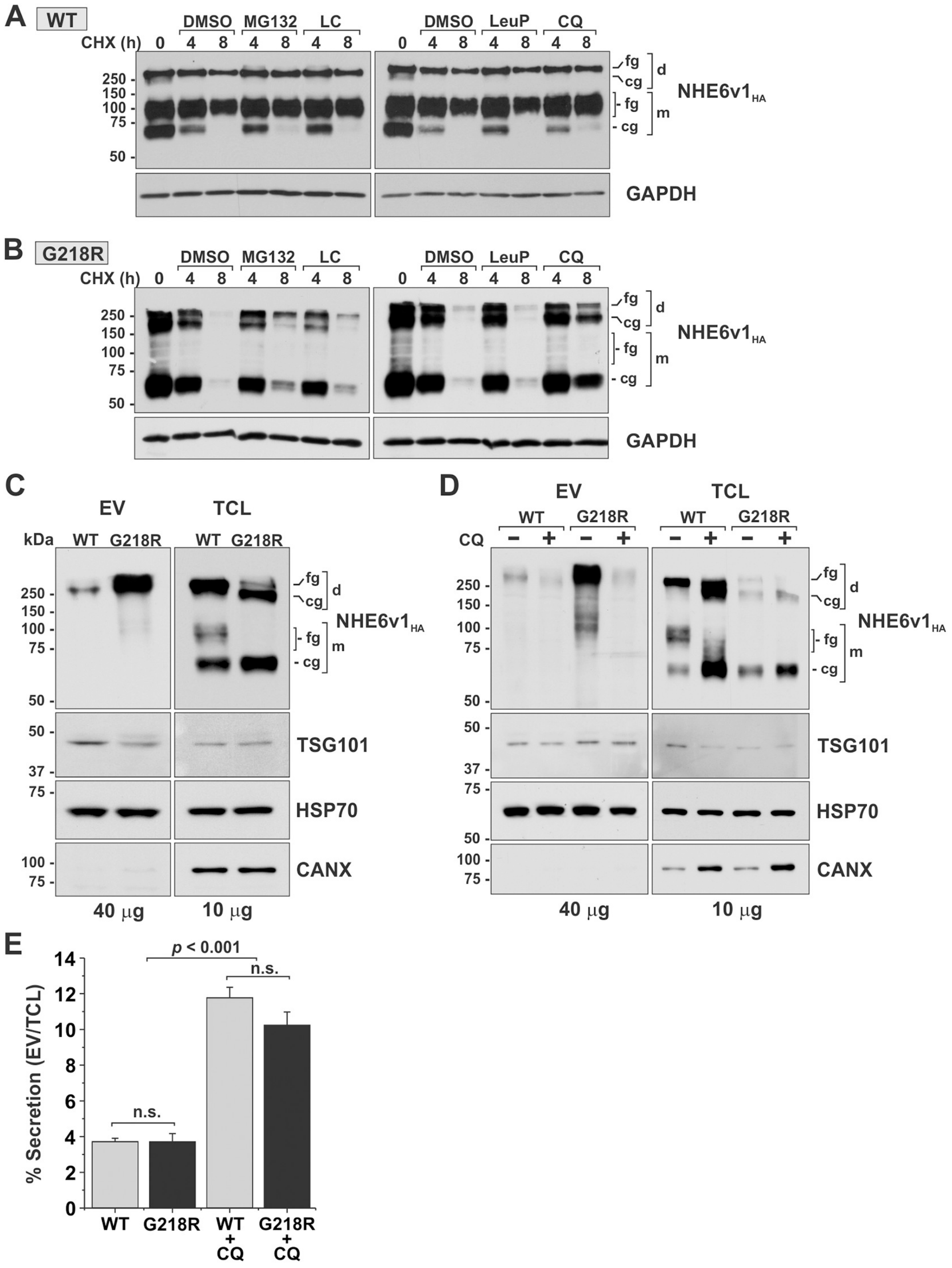

Fig. 3. Effect of proteasomal and lysosomal inhibitor on half-life and cellular clearance of NHE6. AP-1 cells were transiently transfected with (A) WT or (B) G218R for 24 h and then treated with 150 μg/ml cycloheximide for the indicated time points in the presence of diluent (dimethylsulfoxide, DMSO), the proteasomal inhibitors MG-132 (40 μM) or lactacystin (LC, 30 μM) (*left panels*), or the lysosomal inhibitors leupeptin/pepstatin (LeuP, 100 μg/ml) or chloroquine (CQ, 500 μM) (*right panels*). Total cell lysates were analyzed by Western blotting with a mouse monoclonal αHA$_m$ antibody. Membranes were also probed for GAPDH expression as a loading control. The immunoblots are representative of two separate experiments. C, AP-1 cells were transiently transfected with NHE6v1$_{HA}$ WT or G218R for 24 h in serum-free culture media. The media was collected and the extracellular vesicular (EV) membrane fractions were isolated by a differential ultracentrifugation protocol (Greening et al., 2015). The EV fractions as well as total cell lysates (TCL) were analyzed by Western blotting for expression of NHE6v1$_{HA}$ detected with a mouse monoclonal anti-HA (αHA$_m$) antibody. The blots were repeatedly stripped and reprobed for expression of the ESCRT I complex protein TSG101, heat shock protein 70 (HSP70), and calnexin (CANX). D, AP-1 cells transiently expressing WT or G218R at 9 h post-transfection were left untreated (−) or treated (+) with chloroquine (CQ, 250 μM) for an additional 15 h in serum-free culture media. EV and TCL fractions were isolated 24 h post-transfection and analyzed by Western blotting with the indicated antibodies. The amount of protein loaded per lane is indicated at the bottom of the immunoblots. The immunoblots are representative of three independent experiments. E, Quantitation of the total protein levels of the EV fractions expressed as a percentage of its corresponding TCL fractions in the absence or presence of CQ. Values represent the mean ± S.E. (n = 3). Statistical significance was determined by performing a one-way ANOVA with a Tukey post-hoc test; n.s., not significant.

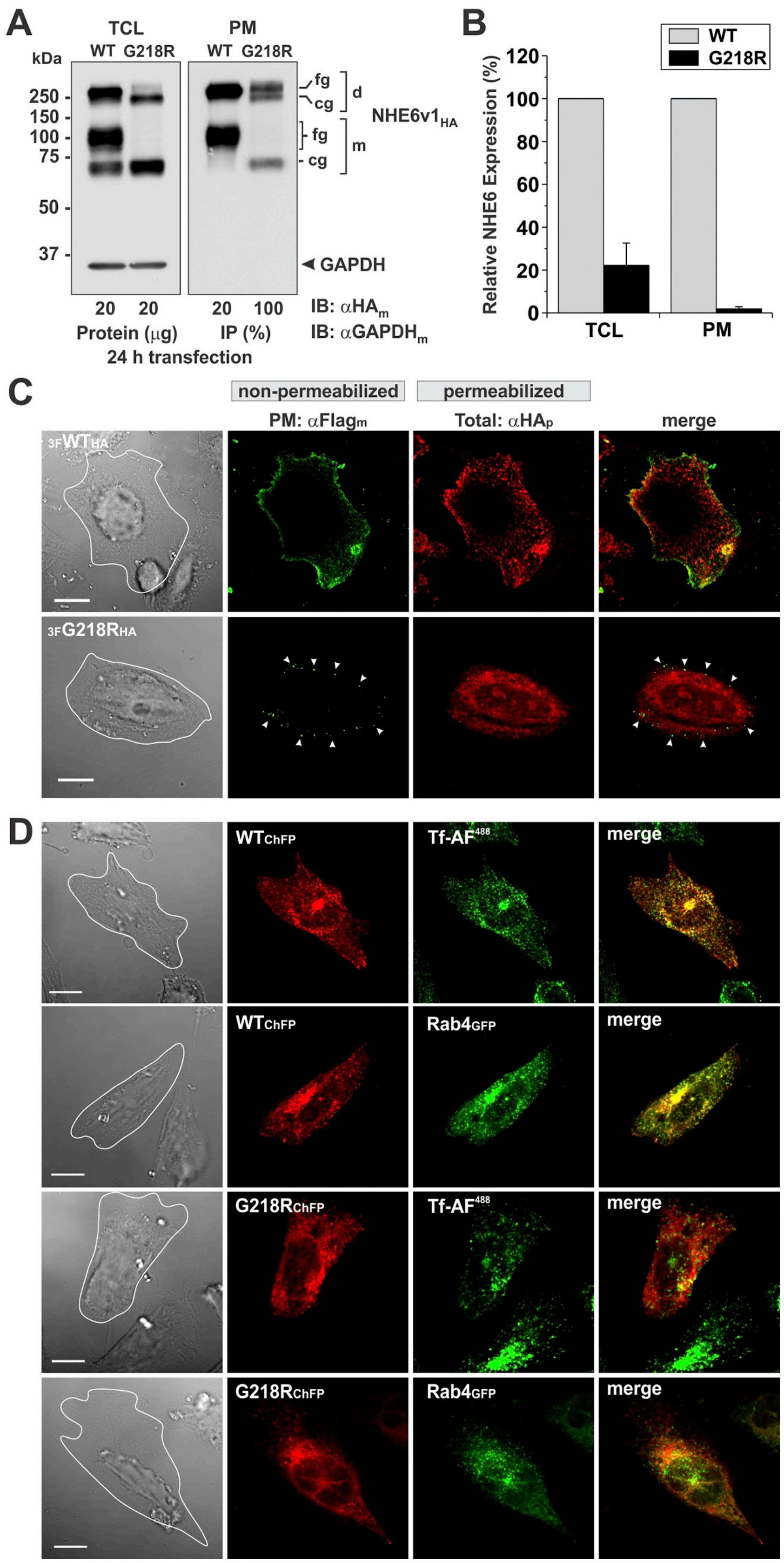

Fig. 4. Membrane trafficking of NHE6 G218R is impaired. A, AP-1 cells were transiently transfected with NHE6v1$_{HA}$ WT or G218R for 24 h and cell surface proteins were labelled with biotin as described in 'Materials and Methods'. Total cell lysates (TCL) were prepared and a small portion representing the total fraction was removed. The remaining supernatants containing equal amounts of total protein for WT and G218R were loaded onto NeutrAvidin® Agarose beads to purify the biotinylated plasma membrane (PM) proteins from the non-biotinylated (intracellular) proteins. For the TCL fraction, aliquots containing 20 µg protein for WT and G218R, were examined by Western blotting (*left panel*). For the plasma membrane (PM) fraction, 20% and 100% of the biotinylated proteins extracted from the TCL of WT and G218R transfectants, respectively, were subjected to Western blotting (*right panel*). Both immunoblots were probed with a mouse monoclonal anti-HA$_m$ antibody (αHA$_m$) to detect NHE6v1$_{HA}$, and an anti-GAPDH$_m$ antibody to assess the purity of the biotinylated PM fraction. B, Densitometric quantification of the relative TCL and PM abundances of WT and G218R. For TCL, the relative protein abundance was expressed as a ratio of NHE6/GAPDH. For the PM level, the relative abundance of the biotinylated G218R was normalized to that of WT, taking into account the differences in protein loading. Values represent the mean ± S.E. (n = 4). C, Cell surface expression of NHE6v1 was also assessed by imaging. To this end, a triple Flag epitope-tag was inserted into the first extracellular loop of NHE6v1$_{HA}$ ($_{3F}$NHE6v1$_{HA}$), as described previously (Ilie et al., 2016). AP-1 cells were transiently transfected (24 h) with WT and G218R, fixed but not permeabilized with detergent to detect only surface expression using a mouse monoclonal anti-Flag antibody (αFlag$_m$). Cells were then permeabilized with saponin to detect total cellular expression using a rabbit polyclonal anti-HA antibody (αHA$_p$) and fluorescence and transmitted light images were acquired using confocal microscopy. Footprints of the transfected cells are indicated as white outlines in the transmitted light images (*far left panels*). D, Representative images of AP-1 cells transiently transfected (24 h) with NHE6v1$_{ChFP}$ WT or G218R individually, or in combination with an organellar marker for recycling endosomes (Rab4$_{GFP}$). Recycling endosomes were also labelled by uptake of Alexa Fluor^{488}-conjugated transferrin (Tf-AF^{488}, 10 µg/ml) for 45 min. *Scale bars* represent 10 µM.

(Fig. 4A-B), consistent with Fig. 2B, however the fraction of G218R at the PM was < 2% of surface WT levels (note the 5-fold higher protein loading in the G218R lane). This indicates there was not only a reduction in protein half-life and abundance, but also impaired delivery and/or retention of the mutant at the cell surface. Moreover, while only fully-glycosylated WT protein was detected in the PM-enriched fraction, the G218R mutant reached the cell surface in both its fully- and core-glycosylated forms.

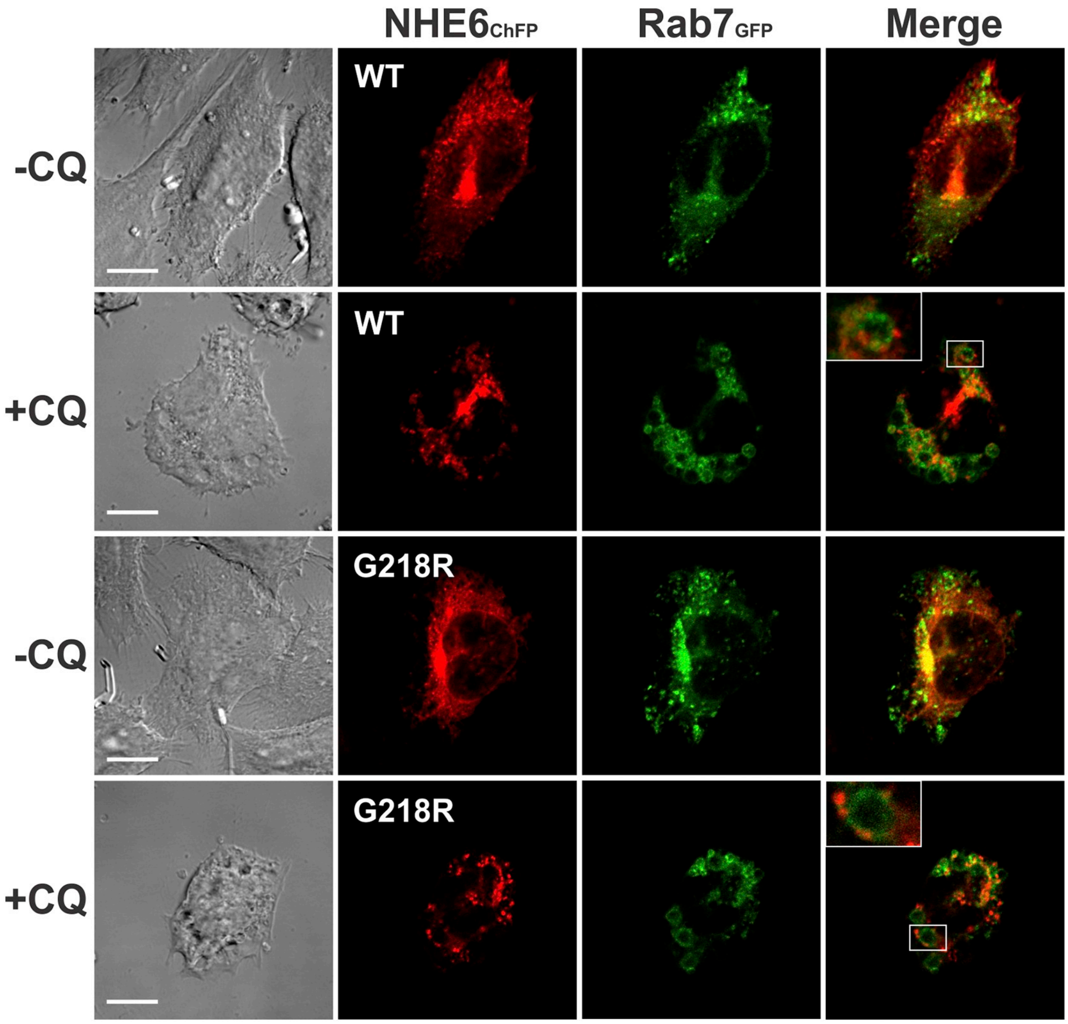

Fig. 5. Chloroquine blocks the fusion of NHE6 G218R-containing vesicles with late endosomes. AP-1 cells were transiently transfected with NHE6v1$_{\text{ChFP}}$ WT or G218R in combination with Rab7$_{\text{GFP}}$ for 9 h, then left untreated (−) or treated (+) with chloroquine (CQ, 250 μM) for an additional 15 h in serum-free culture media. Representative images from two independent experiments are shown. *Scale bars* represent 10 μM.

The distribution of WT and G218R was also verified by fluorescence imaging. A triple Flag epitope-tag (3F) was inserted in the first extracellular loop of NHE6v1$_{\text{HA}}$ ($_{\text{3F}}$NHE6v1$_{\text{HA}}$) as described previously (Ilie et al., 2014). AP-1 cells were transiently transfected (24 h) and fixed but not permeabilized to immuno-detect only surface transporters. Cells were then permeabilized with saponin for detection of total cellular expression using an anti-HA antibody. The WT transporter was distributed on the cell surface in a relatively continuous pattern whereas the G218R mutant had minor punctate immunostaining (Fig. 4C). Intracellularly, the WT transporter was in discrete round-oval and tubulovesicular vesicles throughout the cell as expected. By contrast, the G218R mutant showed a more diffuse, partially reticular, distribution in addition to punctate signals.

To further compare the subcellular distribution of WT and G218R, dual-labelling experiments were performed with C-terminal monomeric Cherry fluorescent protein (ChFP)-tagged constructs of NHE6v1 (*i.e.*, WT$_{\text{ChFP}}$ and G218R$_{\text{ChFP}}$) and organellar markers. The WT$_{\text{ChFP}}$ transporter showed a punctate distribution with substantial accumulation in a compact pericentriolar compartment that overlapped extensively with established markers of recycling endosomes (*i.e.*, Alexa Fluor 488-conjugated transferrin, Tf-AF^{488} and Rab4$_{\text{GFP}}$) (Fig. 4D). As expected, WT$_{\text{ChFP}}$ also showed partial overlap but distinct distribution with markers of the *trans*-Golgi network (TGN) and associated secretory vesicles (*i.e.*; TGN46$_{\text{GFP}}$), clathrin-coated vesicles/early endosomes (*i.e.*; Rab5$_{\text{GFP}}$), and peripheral recycling endosomes (*i.e.*; Rab11$_{\text{myc}}$), whereas minimal overlap was observed with markers of the ER (*i.e.*; CANX), MVB/LEs (*i.e.*; Rab7$_{\text{GFP}}$) and lysosomes (*i.e.*, Lamp1) (Supplementary Fig. S4). Conversely, immunofluorescence signals for the G218R$_{\text{ChFP}}$ mutant were more dispersed and showed very limited colocalization with Tf-AF^{488} and Rab4$_{\text{GFP}}$ (Fig. 4D). Moreover, G218R-expressing cells had visibly reduced uptake and accumulation of Tf-AF^{488} compared to neighboring untransfected cells, suggesting a defect in recycling endosomal trafficking. The G218R$_{\text{ChFP}}$ mutant also showed more discernible overlap with markers of the ER, as well as the TGN, early endosomes and MVB/LE, while overlap with peripheral recycling endosomes or lysosomes was less evident (Supplementary Fig. S5). To test whether the negligible detection of G218R at lysosomes was simply a consequence of lysosomal proteolysis of the fluorophore-tagged transporter, cells were treated with cycloheximide and LeuP for 6 h to track the fate of existing protein while inhibiting lysosomal proteolysis. Blocking *de novo* protein synthesis and lysosomal proteolysis resulted in the detection of both WT and G218R in dispersed vesicles, but did not result in their enrichment in Lamp1-labelled lysosomes (Supplementary Fig. S6). These data are consistent with the biochemical data presented in Fig. 3B where inhibition of lysosomal proteases with LeuP did not block the loss of WT or G218R.

We next examined the effects of chloroquine which, unlike LeuP, did lessen the loss of G218R (see Fig. 3B). Exposure to chloroquine (250 μM, 15 h) induced the formation of abnormally large, membrane-bounded structures that colocalized with Rab7$_{\text{GFP}}$, indicative of malformed MVB/LEs (Fig. 5); results consistent with the vacuologenic effects of chloroquine (Fedorko, 1967). Notably, it largely prevented the signal overlap between G218R$_{ChFP}$ and Rab7$_{GFP}$ that was observed in untreated cells. However, the G218R$_{ChFP}$-containing endosomes were positioned immediately adjacent to the Rab7$_{GFP}$-labelled compartments, as if docked but not fused. Collectively, this subcellular distribution pattern suggests that chloroquine blocks the fusion of G218R-endosomes with MVB/LE.

3.7. G218R-containing endosomes fail to acidify

Acidification of organelles is important for efficient sorting and movement of proteins and lipids along the biosynthetic and endocytic pathways (Casey et al., 2010; Weisz, 2003). To measure intraluminal pH (pH$_v$) of NHE6-containing vesicles, we inserted pHluorin2, a ratiometric pH-sensitive green fluorescent protein (Mahon, 2011), into the first exofacial loop of the WT and mutant NHE6 ($_{pH2}$WT and $_{pH2}$G218R) (Fig. 6A). This insertion did not alter biosynthesis and post-translational maturation (Fig. 6B) or the subcellular distribution (Fig. 6C, *right panel* and *data not shown*) of the proteins. An *in situ* calibration curve of pHluorin2 fluorescence as a function of pH (using cells transfected with $_{pH2}$WT) is presented in Fig. 6C (*left panel*).

To compare the pH$_v$ profiles of $_{pH2}$WT and $_{pH2}$G218R-containing vesicles, AP-1 cells were transiently transfected with each construct for 24 h, and then incubated with cycloheximide for an additional 5 h to block new protein synthesis while allowing the existing WT and G218R to mature biosynthetically and accumulate in vesicles prior to imaging (see examples of imaged vesicles in the insets of Fig. 6D). The pH$_v$ spectrum of vesicles from all $_{pH2}$WT or $_{pH2}$G218R transfected cells analyzed ($n = 12$ cells per construct) display a single-peak Gaussian distribution (Fig. 6D). The average steady-state pH$_v$ of $_{pH2}$WT-containing vesicles was 6.59 ± 0.03 (mean ± S.E., n = 12 cells), which is within the range (pH$_v$ 6.4–6.8) of transferrin-enriched recycling endosomes reported earlier using other approaches (Ilie et al., 2016; Teter et al., 1998; Xinhan et al., 2011; Yamashiro et al., 1984). By contrast, the mean pH$_v$ of $_{pH2}$G218R-containing vesicles was shifted significantly to more alkaline levels; *i.e.*, pH$_v$ 7.09 ± 0.04 (mean ± S.E., n = 12 cells; $p < 0.001$, two-sample Student's *t*-test). This result suggests G218R activity is altered, possibly enhanced (*i.e.*, increased influx of cytoplasmic Na^+ or K^+ in exchange for luminal H^+), which may disrupt recycling endosomal trafficking.

Earlier studies have shown that NHE6 overexpression stimulates the uptake of Tf-TfR complexes into recycling endosomes in a manner that is dependent on its ion transport capabilities (Ilie et al., 2016; Xinhan et al., 2011). As mentioned above, microscopy visualization of Tf-AF^{488} uptake in G218R-expressing cells appears decreased (Fig. 4D). To assess this quantitatively, we used a flow cytometry-based assay to measure the uptake of Alexa Fluor 633-conjugated Tf (Tf-AF^{633}) as a measure of recycling endosomal trafficking. For these experiments, HeLa cells transiently expressing GFP alone or comparable levels of GFP-tagged constructs of WT or G218R (Fig. 6E) were used instead of AP-1 cells because of the significantly higher signal to noise ratio of Tf-AF^{633} uptake, as previously described (Ilie et al., 2016). WT$_{GFP}$-expressing cells exhibited a significant increase in Tf-AF^{633} uptake compared to GFP-transfected controls (WT$_{GFP}$: 171% ± 11, $p < 0.01$, one-sample Student's t-test), whereas this stimulation was attenuated in cells expressing G218R$_{GFP}$ cells (123% ± 5; $p < 0.01$) (Fig. 6F). Collectively, these data indicate that cargo trafficking along the recycling endosomal pathway is compromised in G218R-expressing cells.

3.8. Overexpression of G218R mutant alters dendritic morphology of mouse hippocampal neurons

Previous examination of NHE6 null mice have revealed a crucial role for the transporter in the development and maintenance of axonal and dendritic branching and synapse number of cortical and hippocampal pyramidal neurons (Ouyang et al., 2013). Likewise, analogous changes in the morphology of cultured mouse hippocampal neurons were also observed upon overexpression of NHE6 deletion mutants (p.W370-T372del and p.E287-S288del) (Ilie et al., 2016; Ilie et al., 2014). To investigate whether overexpression of G218R affects the morphological integrity of mature neurons *in vitro*, primary cultures of differentiated hippocampal pyramidal neurons (10–12 days *in vitro,* DIV) prepared from C57BL/6 mice were cotransfected with GFP and ChFP (controls) or GFP plus ChFP-tagged constructs of WT or G218R (*i.e.*, WT$_{ChFP}$ and G218R$_{ChFP}$) and visualized by deconvolution confocal microscopy after 48 h. As shown Fig. 7A, WT$_{ChFP}$-containing vesicles were distributed throughout the soma and neurites in a pattern that mirrors that of endogenous NHE6 (Deane et al., 2013) and the neurons exhibited extensive dendritic arborization comparable to control GFP + ChFP-transfectants. By contrast, in GFP + G218R$_{ChFP}$ co-transfected neurons, the majority of G218R$_{ChFP}$-containing vesicles were concentrated in the soma and primary dendrites, at least as revealed at this low level of resolution. Furthermore, this was associated with striking reductions in higher-order dendritic branching. Using FilamentTracer Imaris software, total dendritic length, surface area and number of branch points of the neurons expressing GFP + G218R$_{ChFP}$ were significantly decreased (ranging from ~26–36% for each parameter) compared to control GFP + ChFP or GFP + WT$_{ChFP}$ (Fig. 7B-D). These observations are consistent with G218R$_{ChFP}$ acting in a dominant-negative manner to suppress endogenous NHE6 function and to disrupt the gross morphology of differentiated neurons.

We next examined whether these changes also correlated with corresponding changes in the distribution of G218R at dendritic spines as well as in spine density and shape, with the latter parameter thought to be a dynamic structural correlate of the strength and maturity of each spine-synapse (*i.e.*, stubby: ambiguous; thin: weak and plastic; mushroom: strong and stable) (Harris et al., 1992). For these analyses, we used the colocalization tool and spine detection and classification algorithm of Imaris. Puncta localized within spines were then tallied based upon their presence in the base, neck, or head subregions of these spines. As shown visually in Fig. 8A-C, the fraction of spines associated with NHE6v1 declined by ~38% for G218R$_{ChFP}$ compared to WT$_{ChFP}$ (WT$_{ChFP}$, 79.6% ± 2.0; G218R$_{ChFP}$, 49.7% ± 4.0; $p < 0.0001$). Moreover, of the NHE6v1-associated spines, there was a significant decrease (~62%) in the accumulation of G218R$_{ChFP}$ in the head (WT$_{ChFP}$, 42.5% ± 2.0; G218R$_{ChFP}$, 16.1% ± 3.7; $p < 0.0001$) and a reciprocal increase (~63%) at the base (WT$_{ChFP}$, 46.1% ± 2.4; G218R$_{ChFP}$, 75.3% ± 5.3; $p < 0.0001$) of spines compared to WT$_{ChFP}$, whereas no change was detected in the neck subregion. These changes coincided with a marked reduction in total spine density of G218R$_{ChFP}$-transfected neurons compared to control GFP + ChFP or GFP + WT$_{ChFP}$ transfectants (25% and 34%, respectively) (# spines/μm dendrite: ChFP, 0.91 ± 0.06; WT$_{ChFP}$, 1.02 ± 0.05; G218R$_{ChFP}$, 0.68 ± 0.04; $p < 0.0001$) (Fig. 8D). This decrease was attributed solely to the loss of mature mushroom-shaped spines (ChFP, 0.35 ± 0.03; WT$_{ChFP}$, 0.40 ± 0.02; G218R$_{ChFP}$, 0.17 ± 0.01) and coincided with a several-fold increase in the density of immature filopodial-like protrusions (# filopodia/μm dendrite: ChFP, 0.012 ± 0.006; WT$_{ChFP}$, 0.005 ± 0.005; G218R$_{ChFP}$, 0.064 ± 0.014; $p < 0.01$) (Fig. 8E). Thus, in addition to gross changes in neuronal morphology, expression of G218R selectively impairs the formation of mature synapses.

To compare the steady-state pH$_v$ of WT and G218R-containing vesicles, the neurons were transiently transfected with the $_{pH2}$WT and $_{pH2}$G218R constructs for 24 h, but in this instance were not further treated with cycloheximide as this was not well tolerated by the G218R-expressing cells. To ensure pH measurements were confined to endosomes (and not newly synthesized NHE6v1 in the ER), image analyses were focused primarily on discrete punctate in dendritic shafts and spines (see insets of Fig. 8F). The average steady-state pH$_v$ of $_{pH2}$WT-containing vesicles was 6.79 ± 0.02, whereas the mean pH$_v$ of $_{pH2}$G218R-containing vesicles was shifted significantly to more alkaline levels; *i.e.*, pH$_v$ 7.14 ± 0.02 ($p < 0.001$) (Fig. 8F). These findings are

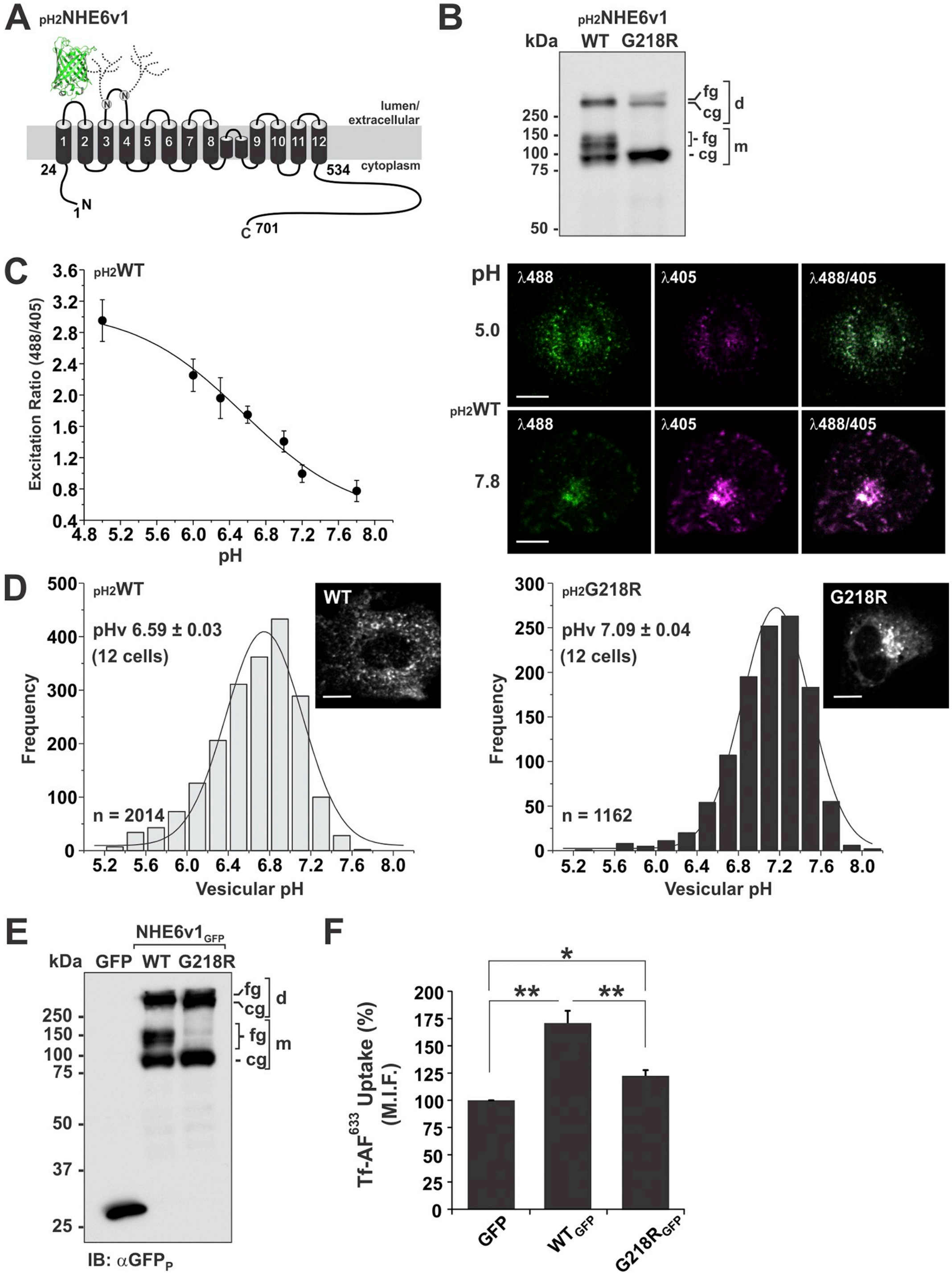

Fig. 6. Acidification and cargo trafficking of NHE6 G218R-containing vesicles are impaired. A, Illustration of NHE6v1 containing the pH-sensitive pHluorin2 (pH 2) inserted in its first extracellular loop ($_{pH2}$NHE6v1). B, Representative Western blot of total cell lysates of AP-1 cells transient expressing (24 h) $_{pH2}$WT or $_{pH2}$G218R. The immunoblot was probed with a polyclonal anti-GFP antibody (αGFP$_P$). C, Vesicular pH was measured by single-cell fluorescence ratiometric imaging analysis (FRIA) at 37 °C using a Zeiss LSM 780 confocal microscope as described in 'Materials and Methods'. The *left panel* shows the *in situ* calibration curve of pH 2 fluorescence (excitation ratio 488/405) as a function of vesicular pH performed by *in situ* clamping of vesicular pH between 5 and 7.8. The *right panel* shows representative fluorescence images of AP-1 cells expressing $_{pH2}$WT when excited at 488 nm (green) and 405 nm (pseudo-coloured magenta) as well as the merged (488/405) images when clamped at pH 5 and 7.8. D, Graphical plot of the intraluminal pH of $_{pH2}$WT- and $_{pH2}$G218R-containing vesicles. The experiment was repeated 3 times and the plots show the frequency of vesicles as a function their intraluminal pH analyzed from 12 cells for each construct. The total number of vesicles analyzed (n) and the average vesicular pH (pH$_v$) (mean ± S.E.) are indicated in the plots. Insets shows representative images of $_{pH2}$WT- and $_{pH2}$G218R-containing vesicles in transfected cells. E, HeLa cells were transiently transfected (24 h) with GFP, NHE6v1$_{GFP}$ WT or G218R. Total cell lysates were prepared and analyzed by Western blotting using a polyclonal anti-GFP (αGFP$_P$) antibody. F, Uptake of Tf-AF^{633} was monitored in HeLa cells expressing GFP, WT$_{GFP}$ or G218R$_{GFP}$. Median fluorescence intensity (M.I.F.) of Tf-AF^{633} was measured in 10^4 GFP-positive cells by flow cytometry. Data were normalized and represent mean ± S.E. (n = 4). Significance was established using a Student's *t*-test, *$p < 0.05$, **$p < 0.01$. (For interpretation of the references to colour in this figure legend, the reader is referred to the web version of this article.) (I'm not sure i understand what is meant by this comment. What is the reader being referred to?)

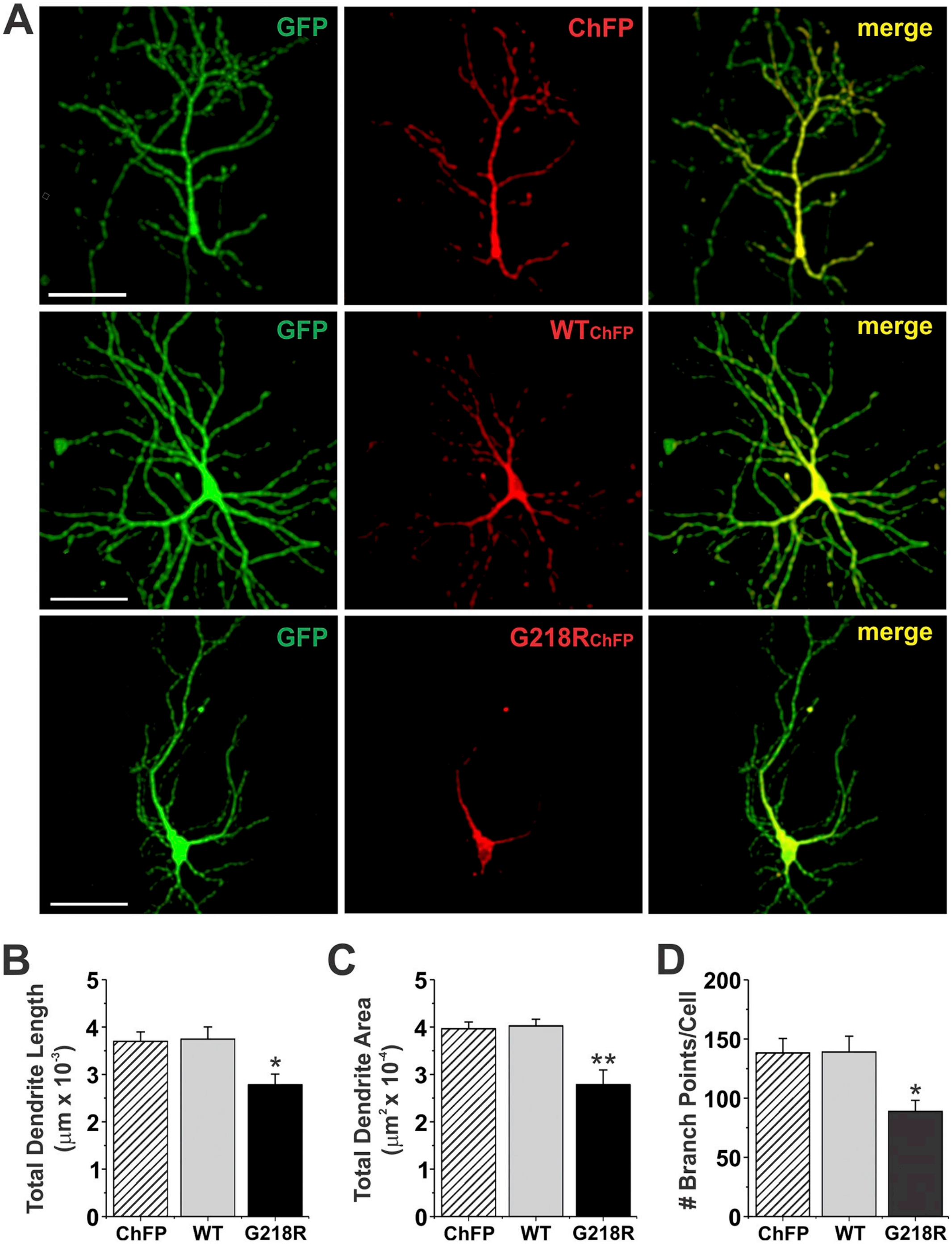

Fig. 7. Heterologous expression of G218R decreases the complexity of dendritic arborisation in mouse hippocampal neurons. A, Confocal images of primary hippocampal pyramidal neurons co-transfected with cytosolic enhanced GFP (to visualize cell morphology) and monomeric cherry fluorescent protein (ChFP) (as a transfection control), or with GFP and ChFP-tagged NHE6 WT or G218R (WT_{ChFP} and $G218R_{ChFP}$, respectively). Forty-eight h post-transfection, cells were fixed in 4% paraformaldehyde, mounted onto glass slides, and examined by confocal microscopy. Images show each channel separately and merged. B-D, Quantification of parameters related to neuronal branching, including the sums of total dendritic length (B) and area (C), as well as the total number of branch points per cell (D) using the FilamentTracer plug-in module from Imaris Software. Values represent the mean ± S.E. of 3 separate experiments (n = 5 neurons for each condition/experiment). $^{*}p < 0.05$; $^{**}p < 0.01$, one-way ANOVA with a Bonferroni post-hoc test. Scale bar: 60 μm.

comparable to results obtained in AP-1 cells.

4. Discussion

In this report, we describe a unique SLC9A6/NHE6 missense variant (p.G218R) associated with Christianson Syndrome that results in an apparent gain-of-function, as manifested by hypoacidification (*i.e.*, alkalinization) of G218R-endosomes. Despite this ostensible “gain-of-function”, the transporter was nonetheless recognized as defective as evidenced by its elevated state of ubiquitination and rapid expulsion from the cell by exosomal release. A schematic representation depicting these events is illustrated in Fig. 9. This contrasts with other mutations that cause total loss-of-function and correlate with overacidification and premature activation of acid proteases within endosomes and/or

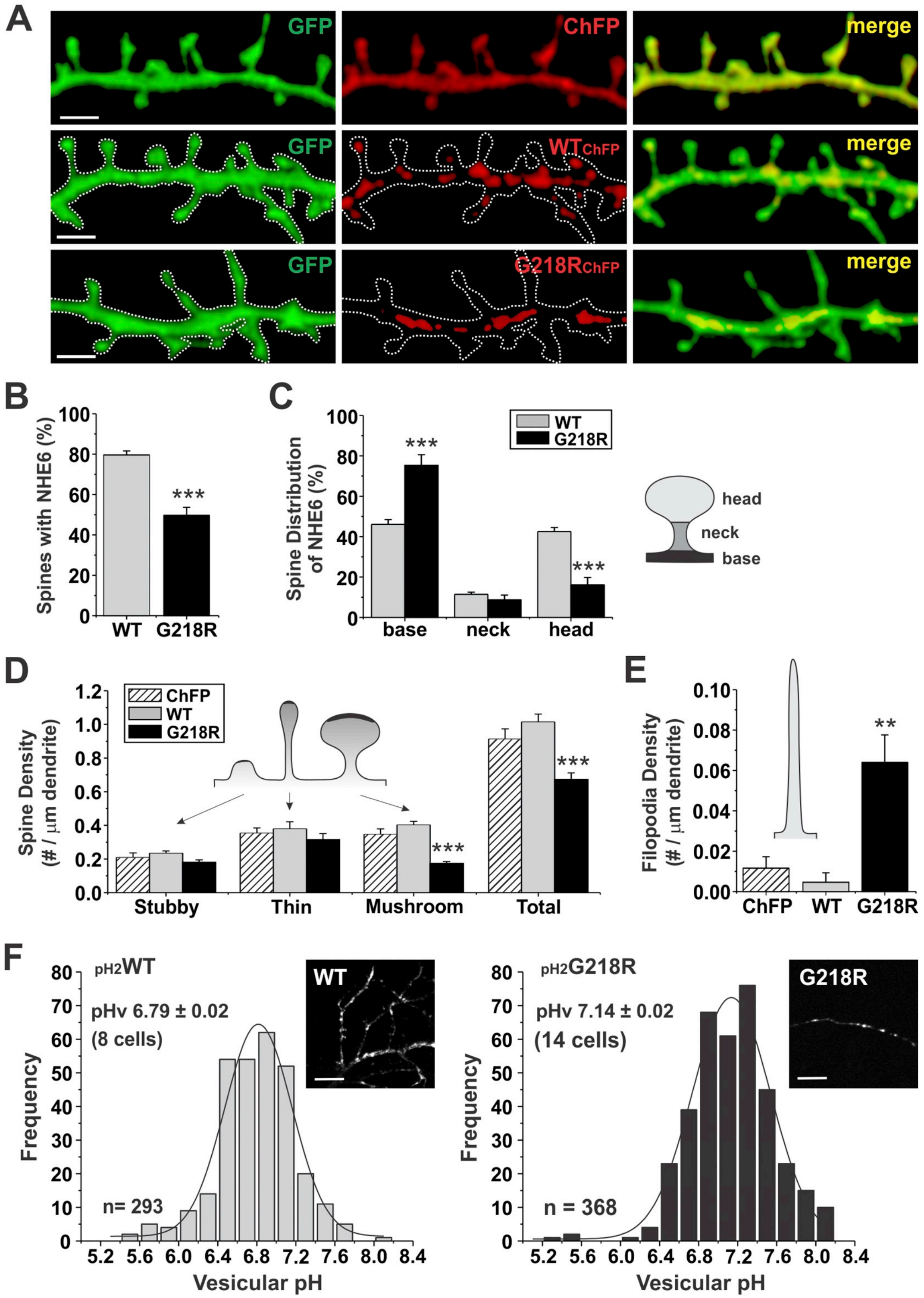

Fig. 8. Heterologous expression of G218R reduces the density of mature dendritic spines and increases appearance of filopodia.

A, Representative confocal images of secondary and tertiary dendrites of 14+ DIV primary hippocampal neurons co-transfected with enhanced GFP and ChFP alone or with GFP and WT$_{ChFP}$ or G218R$_{ChFP}$. GFP and ChFP channels are shown individually and merged. Scale bar: 2 μm. B, Quantification of the fraction of spines (mean ± S.E.) containing puncta of transfected WT$_{ChFP}$ or G218R$_{ChFP}$ of all spines analyzed for each transfection condition. C, Quantification of the proportion (mean ± S.E.) of spine-localized puncta of overexpressed WT$_{ChFP}$ or G218R$_{ChFP}$ in each major spine subregion. *i.e.* base (black), neck (dark gray), and head (light gray). D-E, Quantification of the density (mean ± S.E.) of each major spine subtype, *i.e.* stubby, mushroom, and thin (D), as well as immature filopodia-like structures (E). Data were collected from 3 separate experiments: GFP control: n = 214 spines and 2 filopodia along 234 μm of dendrite from 8 cells; WT$_{ChFP}$: n = 234 spines and 1 filopodia along 236 μm of dendrite from 8 cells; G218R$_{ChFP}$: n = 158 spines and 15 filopodia along 232 μm of dendrite from 8 cells. **: $p < 0.01$; ***: $p < 0.0001$, one-way ANOVA with Bonferroni post-hoc test for all comparisons except filopodia (Kruskall-Wallis test with Dunns post-hoc). F, Graphical plot of the intraluminal pH of $_{pH2}$WT- and $_{pH2}$G218R-containing vesicles in transfected primary mouse hippocampal neurons. The experiment was repeated 3 times and the plots show the frequency of vesicles as a function their intraluminal pH (pH$_v$) analyzed from 8 to 14 cells for each construct. The total number of vesicles analyzed and the average pH values (mean ± S.E.) are indicated in the plots. Insets shows representative images of $_{pH2}$WT- and $_{pH2}$G218R-containing vesicles in neurites of transfected cells.

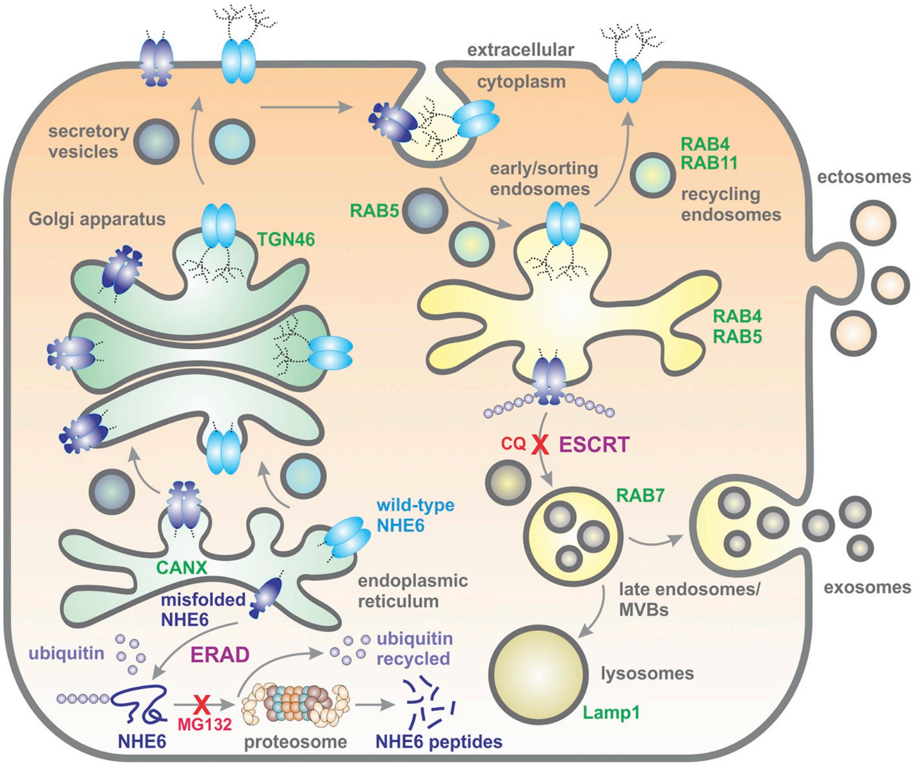

Fig. 9. Cellular processing and membrane trafficking of NHE6. Schematic representation of the cellular processing of NHE6v1 WT and G218R along the exocytic and endocytic pathways. Nascent transporters are cotranslationally inserted into the ER membrane where they undergo *N*-linked core glycosylation. Upon proper folding and dimer assembly, the WT transporter is exported to the Golgi where it is subject to additional complex glycosylation, prior to export to the plasma membrane (PM). By contrast, the G218R transporter is more prone to misfolding at the ER and is targeted for ubiquitination and proteasomal degradation (*i.e.*, ERAD pathway), effects that are partially blocked by proteasomal inhibitors such as MG132 (and lactacystin, *not shown*). However, a significant fraction of G218R is able to assemble as a homodimer and traffic through the Golgi to the PM, though complex glycosylation is largely impaired. PM-resident WT is internalized and normally recycled back to the PM. By contrast, G218R is recognized by the peripheral quality control machinery (*i.e.*, ESCRT pathway) and targeted to late endosomes/multivesicular bodies (MVBs) that subsequently fuse with the PM and release their intraluminal vesicles (or exosomes) containing NHE6 into the extracellular milieu. The lysosomotropic agent chloroquine (CQ) blocks the transfer of G218R from early/sorting endosomes to late endosomes/ MVBs.

expansion of the lysosomal compartment (Ilie et al., 2016; Ouyang et al., 2013; Roxrud et al., 2009). Despite these differences, in both cases there is a net loss of NHE6 protein which correlated with similar deleterious consequences on endosomal trafficking and neuronal morphology (Ilie et al., 2016; Ouyang et al., 2013; Roxrud et al., 2009). Clinically, the proband exhibited the vast majority of symptoms observed in CS patients devoid of NHE6 expression, with the exception of underdeveloped but stable motor skills. The significance, if any, of this latter feature in relation to the G218R mutation is unclear. It could be due to the variable degree and onset of motor regression in CS patients as well as other genetic modifier effects.

The G218R mutation compromises the structure-function integrity of the transporter. While the mutant transporter was capable of assembling as a homodimer, its level of complex glycosylation was significantly diminished and correlated with enhanced ubiquitination. A fraction of ubiquitinated G218R was subjected to proteasomal proteolysis, but contrary to expectations the bulk of ubiquitinated G218R was secreted in EVs rather than targeted to lysosomes. EVs are generated by virtually all cells and represent a heterogeneous population of vesicles that include nanoscale vesicles or exosomes (~30–100 nm in diameter) spawned by invagination and abscission of the limiting membrane of MVB/LEs and subsequently expelled after fusion with the PM, and larger-sized vesicles (often termed microparticles, microvesicles or ectosomes that range in size from ~100–1000 nm) formed by the outward budding and shedding of discrete subdomains of the PM (Colombo et al., 2014). Cellular discharge of EVs was initially described as a unique non-degradative route for removing unwanted or damaged macromolecules (Johnstone et al., 1987). However, subsequent studies have demonstrated that EVs also serve as a significant mode of intercellular communication under different physiological and pathophysiological conditions due to their ability to fuse with and transfer biologically active molecules to neighboring or more distally located cells (Budnik et al., 2016; Colombo et al., 2014; Simons and Raposo, 2009). While our isolation methods did not distinguish between exosomes and ectosomes, the partial signal overlap of G218R$_{\text{ChFP}}$ with Rab7$_{\text{GFP}}$-labelled MVB/LEs suggests that exosomal release is the likely route for cellular clearance. Thus, CS can be added to a growing list of neurodegenerative diseases, such as Alzheimer's, Parkinson's and amyotrophic lateral sclerosis, associated with exosomal release of defective proteins (Levy, 2017; Rajendran et al., 2014; Vella et al., 2016).

The mechanisms underlying the enhanced accumulation of ubiquitinated G218R in MVB/LEs destined to fuse with the PM rather than merge with lysosomes (*i.e.*, secretory *versus* degradative MVB/LEs, respectively) is unknown. However, the coexistence of discrete subpopulations of MVB/LEs within cells is supported by biochemical and ultrastructural studies. For instance, intraluminal vesicles of MVB/LEs released as exosomes are highly enriched in cholesterol and the sphingolipids ceramide, sphingomyelin and ganglioside GM3; components associated with lipid raft microdomains in the plasma membrane (Mobius et al., 2003; Trajkovic et al., 2008; Wubbolts et al., 2003). Inhibition of ceramide formation from sphingomyelin by pharmacological antagonists or RNAi depletion of neutral sphingomyelinase 2 (nSMase2), which has an optimum pH of 7.4, reduces release of exosomes without impairing lysosomal function (Trajkovic et al., 2008). By contrast, intraluminal membranes of another subpopulation of MVB/LE that progress to lysosomes are largely devoid of cholesterol but positive for a unique phospholipid, bis(monoacylglycero)phosphate (BMP) - also known as lysobisphosphatidic acid (LBPA)(Kobayashi et al., 1998; Mobius et al., 2003), that is absent from exosomes (Wubbolts et al., 2003). Interestingly, the intrinsic biophysical properties of BMP/LBPA promote the formation of MVB/LE internal vesicles in a manner that is dependent on acidic pH and Alix, an ESCRT-associated protein (Hayakawa et al., 2007; Matsuo et al., 2004). Thus, these findings provide some evidence for the coexistence of at least two separate subpopulations of MVB/LEs that can be distinguished not only by their lipid composition, but also by their intraluminal pH (*i.e.*, acidic *versus* alkaline). Based on these observations, we speculate that the more alkaline environment of G218R-containing early endosomes may favour ceramide production and the sequestering of G218R into lipid raft-enriched intraluminal vesicles of MVB/LEs destined for secretion as exosomes.

This raises the question of whether intraluminal pH plays a more direct role in regulating the trafficking fate of distinct subpopulations of MVB/LE. This possibility is supported by studies showing that pathogen-mediated neutralization of endolysosomal pH in bladder epithelial cells acts as a critical signal that selectively activates the transient receptor potential mucolipin-3 (TRPML3) cation channel to release their luminal stores of Ca^{2+}, triggering cellular expulsion rather than internal degradation of bacteria-containing exosomes by lysosomes (Miao et al., 2015). Conversely, low luminal pH is thought to potentiate Ca^{2+} conductance of the endolysosomal TRPML1 channel and promote lysosomal biogenesis and function (Cheng et al., 2010; Xu et al., 2007). Thus, differential regulation of endolysosomal pH and pH-sensitive Ca^{2+} channels may play important roles in determining whether vesicle-associated cargo is destined for secretion or degradation, though the precise sorting mechanisms remain obscure.

Consistent with the above notion, we found that chloroquine which non-selectively neutralizes acidic endomembrane compartments enhanced the bulk release of EVs from CHO/AP-1 cells. However, while it fostered release of EVs, it also concomitantly blocked the extracellular export of G218R by preventing the fusion of G218R-vesicles with enlarged $Rab7_{GFP}$-labelled MVB/LEs. This effect agrees with earlier observations that chloroquine causes accumulation of endocytosed macromolecules in early endosomes that otherwise would be transferred to MVB/LEs and lysosomes (Lippincott-Schwartz and Fambrough, 1987; Stenseth and Thyberg, 1989). Other studies have also shown that dissipation of the proton gradient by inhibiting the vacuolar H^+-ATPase with bafilomycin preferentially abrogated protein trafficking between the early and late endosomal compartments (Baravalle et al., 2005), whereas internalization and recycling of membrane cargo back to the cell surface were slowed but not blocked (Presley et al., 1997). Why this particular step in endomembrane trafficking along the degradative pathway is especially sensitive to agents that disrupt intraluminal acidification is not fully understood. However, emerging evidence has revealed that the vacuolar H^+-ATPase operates not only as a pH-regulator, but also as a platform to recruit components of the vesicular trafficking machinery (*i.e.,* small GTPase Arf6 and its associated guanine nucleotide exchange factor ARNO) in an intra-endosomal pH-dependent manner (Hurtado-Lorenzo et al., 2006). Notably, these interactions were found to be critical for endosomal trafficking between the early and late endosomal compartments, but not the recycling endosomal pathway. Accordingly, this behaviour could explain how chloroquine preferentially blocked the extracellular release of G218R, but did not impair the secretions of EV-associated TSG101 or HSP70 which may be sorted to MVB/LE independently of early endosomal delivery. Thus, bulk release of EVs at later stages of exocytosis do not appear to be dependent on luminal acidification, but instead may be stimulated by alkalinization.

Under steady-state conditions, NHE6 operates as an alkalinizing mechanism (*i.e.*, cytoplasmic Na^+ or K^+ influx in exchange for luminal H^+) to counterbalance the acidifying effects of the vacuolar H^+-ATPase, achieving an intraluminal pH in the range of ~6.4–6.6 in various cell types, including fibroblasts (Ilie et al., 2016; Xinhan et al., 2011), epithelia (Ohgaki et al., 2010) and neurons (Ouyang et al., 2013). Downregulating NHE6 expression or catalytic activity result in overacidification of recycling endosomes which, by an ill-defined mechanism, reduces their shuttling to and from the PM (Ilie et al., 2016; Ohgaki et al., 2010; Ouyang et al., 2013; Xinhan et al., 2011). Significantly, this impaired vesicle trafficking was associated with loss of epithelial apical cell polarity (Ohgaki et al., 2010) and neuronal degeneration and death (Ilie et al., 2016; Ouyang et al., 2013; Stromme et al., 2011). In contrast to loss-of-function mutations, we found that G218R-containing endosomes where considerably more alkaline compared to WT-endosomes in both AP-1 cells and primary cultures of mouse hippocampal neurons. While the precise consequences of this mutation on the kinetic properties of NHE6 will require further study, the elevated pH_v could simply be explained by a gain-of-function, though other mechanisms are possible. For instance, the mutation could result in uncoupled H^+ efflux in a manner analogous to uncoupled Cl^- conductance for mutated forms of endosomal electrogenic $2Cl^-/1H^+$ exchangers of the CLC family (Scheel et al., 2005). Notwithstanding, this mutation still negatively impacted recycling endosomal trafficking in both cell types.

In hippocampal neurons, G218R overexpression resulted in pronounced reductions in dendritic arborization and spine density, with a selective loss of mature mushroom-shaped spines and the emergence of immature filopodial-like protrusions. These morphological alterations closely resemble effects observed when disrupting components of the cytoplasmic molecular machinery (*i.e.*, Rab11, syntaxin13, and EHD1/Rme1) that control the trafficking of recycling endosomes, including rapid declines in dendritic spine size and density and abolition of AMPAR trafficking and long-term potentiation (LTP), a well-established cellular model of learning and memory (Park et al., 2006). The colocalization of NHE6 with AMPAR (Deane et al., 2013) and TRKB (Ouyang et al., 2013) in recycling endosomes suggests that NHE6 may function as a molecular link between the fine control of endosomal pH and trafficking signals that direct cargo needed for neurons to mature, function and survive.

In conclusion, disruption of NHE6 activity through either loss- or gain-of-function impairs optimal recycling endosomal function and thus may explain many of the neurodevelopmental and neurodegenerative symptoms associated with the pathophysiology of CS.

Ethics approval and consent to participate

For all family members, informed consent was obtained for participation in this study according to relevant institutional and national guidelines and regulations. All procedures for animal handling were approved by the McGill University Facility Animal Care Committee (FACC) and carried out in full compliance with the Policies and Guidelines of the Canadian Council on Animal Care (CCAC).

Availability of data and materials

The genetic data were deposited in the DECIPHER database (patient 368,102; http://decipher.sanger.ac.uk). All other data generated or analyzed during this study are included in this published article and its supplementary data file.

Competing interests

The authors declare that they have no competing interests.

Funding

This work was supported by research funds from the Canadian Institutes of Health Research (CIHR) (MOP-111191, PJT-155976) and McGill Faculty of Medicine to J.O., and the CIHR (MOP-86724) to R.A.M.. A.Y.L.G. is the recipient of an Alexander Graham Bell Canada Graduate Scholarship.

Authors' contributions

Y·H-H. and M.J.V.H. performed the clinical diagnosis and genetic testing of the CS patient. A.I. and A.B. performed molecular, biochemical and data analyses; A.I. and A.Y.L.G. performed the immunofluorescence imaging studies; J.P. and A.M.B. performed the structure homology modelling of NHE6v1; A.I., R.A.M. and JO designed, supervised and coordinated different aspects of the experiments and data analyses; A.I. and J.O. wrote the manuscript; all authors critically discussed results, revised and approved the final version of the manuscript.

Acknowledgements

The authors wish to express sincere appreciation to Dr. John Hanrahan (McGill University) for critically reviewing the manuscript. We are grateful for the services provided by McGill Life Sciences Advanced BioImaging Facility and the Flow Cytometry Facility, and Genome Québec for DNA sequencing; platforms supported by funding from the Canadian Foundation for Innovation.

Appendix A. Supplementary data

Supplementary data to this article can be found online at https://doi.org/10.1016/j.nbd.2018.10.002.

References

Baravalle, G., et al., 2005. Transferrin recycling and dextran transport to lysosomes is differentially affected by bafilomycin, nocodazole, and low temperature. Cell Tissue Res. 320, 99–113.

Bergeron, J.J., et al., 1994. Calnexin: a membrane-bound chaperone of the endoplasmic reticulum. Trends Biochem. Sci. 19, 124–128.

Brett, C.L., et al., 2002. Human Na^+/H^+ exchanger isoform 6 is found in recycling endosomes of cells, not in mitochondria. Am. J. Physiol. Cell Physiol. 282, C1031–C1041.

Budnik, V., et al., 2016. Extracellular vesicles round off communication in the nervous system. Nat. Rev. Neurosci. 17, 160–172.

Buschow, S.I., et al., 2005. Exosomes contain ubiquitinated proteins. Blood Cells Mol. Dis. 35, 398–403.

Calinescu, O., et al., 2017. Lysine 300 is essential for stability but not for electrogenic transport of the Escherichia coli NhaA Na^+/H^+ antiporter. J. Biol. Chem. 292, 7932–7941.

Casey, J.R., et al., 2010. Sensors and regulators of intracellular pH. Nat. Rev. Mol. Cell Biol. 11, 50–61.

Cheng, X., et al., 2010. Mucolipins: Intracellular TRPML1-3 channels. FEBS Lett. 584, 2013–2021.

Christianson, A.L., et al., 1999. X linked severe mental retardation, craniofacial dysmorphology, epilepsy, ophthalmoplegia, and cerebellar atrophy in a large South African kindred is localised to Xq24-q27. J. Med. Genet. 36, 759–766.

Coincon, M., et al., 2016. Crystal structures reveal the molecular basis of ion translocation in sodium/proton antiporters. Nat. Struct. Mol. Biol. 23, 248–255.

Colombo, M., et al., 2013. Analysis of ESCRT functions in exosome biogenesis, composition and secretion highlights the heterogeneity of extracellular vesicles. J. Cell Sci. 126, 5553–5565.

Colombo, M., et al., 2014. Biogenesis, secretion, and intercellular interactions of exosomes and other extracellular vesicles. Annu. Rev. Cell Dev. Biol. 30, 255–289.

Deane, E.C., et al., 2013. Enhanced recruitment of endosomal Na^+/H^+ Exchanger NHE6 into dendritic spines of hippocampal pyramidal neurons during NMDA receptor-dependent long-term potentiation. J. Neurosci. 33, 595–610.

Fagerberg, L., et al., 2014. Analysis of the human tissue-specific expression by genome-wide integration of transcriptomics and antibody-based proteomics. Mol. Cell. Proteomics 13, 397–406.

Fedorko, M., 1967. Effect of chloroquine on morphology of cytoplasmic granules in maturing human leukocytes–an ultrastructural study. J. Clin. Invest. 46, 1932–1942.

Firth, H.V., et al., 2009. DECIPHER: Database of Chromosomal Imbalance and Phenotype in Humans using Ensembl Resources. Am. J. Hum. Genet. 84, 524–533.

Gilfillan, G.D., et al., 2008. SLC9A6 mutations cause X-linked mental retardation, microcephaly, epilepsy, and ataxia, a phenotype mimicking Angelman syndrome. Am. J. Hum. Genet. 82, 1003–1010.

Greening, D.W., et al., 2015. A protocol for exosome isolation and characterization: evaluation of ultracentrifugation, density-gradient separation, and immunoaffinity capture methods. Methods Mol. Biol. 1295, 179–209.

Harris, K.M., et al., 1992. Three-dimensional structure of dendritic spines and synapses in rat hippocampus (CA1) at postnatal day 15 and adult ages: implications for the maturation of synaptic physiology and long-term potentiation. J. Neurosci. 12, 2685–2705.

Hayakawa, T., et al., 2007. pH-dependent formation of membranous cytoplasmic body-like structure of ganglioside G(M1)/bis(monoacylglycero)phosphate mixed membranes. Biophys. J. 92, L13–L16.

Hurtado-Lorenzo, A., et al., 2006. V-ATPase interacts with ARNO and Arf6 in early endosomes and regulates the protein degradative pathway. Nat. Cell Biol. 8, 124–136.

Ilie, A., et al., 2014. Impaired posttranslational processing and trafficking of an endosomal Na^+/H^+ exchanger NHE6 mutant ($D^{370}WST^{372}$) associated with X-linked intellectual disability and autism. Neurochem. Int. 73, 192–203.

Ilie, A., et al., 2016. A Christianson syndrome-linked deletion mutation ($D^{287}ES^{288}$) in SLC9A6 disrupts recycling endosomal function and elicits neurodegeneration and cell death. Mol. Neurodegener. 11.

Johnstone, R.M., et al., 1987. Vesicle formation during reticulocyte maturation. Association of plasma membrane activities with released vesicles (exosomes). J. Biol. Chem. 262, 9412–9420.

Kobayashi, T., et al., 1998. A lipid associated with the antiphospholipid syndrome regulates endosome structure and function. Nature 392, 193–197.

Kowal, J., et al., 2016. Proteomic comparison defines novel markers to characterize heterogeneous populations of extracellular vesicle subtypes. Proc. Natl. Acad. Sci. U. S. A. 113, E968–E977.

Kozachkov, L., et al., 2007. Functional and structural interactions of the transmembrane domain X of NhaA, Na^+/H^+ antiporter of Escherichia coli, at physiological pH. Biochemistry 46, 2419–2430.

Landau, M., et al., 2007. Model structure of the Na^+/H^+ exchanger 1 (NHE1): functional and clinical implications. J. Biol. Chem. 282, 37854–37863.

Le Bivic, A., et al., 1989. Vectorial targeting of apical and basolateral plasma membrane proteins in a human adenocarcinoma epithelial cell line. Proc. Natl. Acad. Sci. U. S. A. 86, 9313–9317.

Lee, C., et al., 2013. A two-domain elevator mechanism for sodium/proton antiport. Nature 501, 573–577.

Levy, E., 2017. Exosomes in the diseased brain: first insights from in vivo Studies. Front. Neurosci. 11, 142.

Li, X., et al., 2014. Functional role of arginine 425 in the mammalian Na^+/H^+ exchanger. Biochem. Cell Biol. 92, 541–546.

Lippincott-Schwartz, J., Fambrough, D.M., 1987. Cycling of the integral membrane glycoprotein, LEP100, between plasma membrane and lysosomes: kinetic and morphological analysis. Cell 49, 669–677.

Maeda, Y., Kinoshita, T., 2010. The acidic environment of the Golgi is critical for glycosylation and transport. Methods Enzymol. 480, 495–510.

Maes, M., et al., 2012. Revealing the ligand binding site of NhaA Na^+/H^+ antiporter and its pH dependence. J. Biol. Chem. 287, 38150–38157.

Mahon, M.J., 2011. pHluorin2: an enhanced, ratiometric, pH-sensitive green florescent protein. Adv. Biosci. Biotechnol. 2, 132–137.

Masurel-Paulet, A., et al., 2016. A new family with an SLC9A6 mutation expanding the phenotypic spectrum of Christianson syndrome. Am. J. Med. Genet. A 170, 2103–2110.

Matsuo, H., et al., 2004. Role of LBPA and Alix in multivesicular liposome formation and endosome organization. Science 303, 531–534.

Maxfield, F.R., 1982. Weak bases and ionophores rapidly and reversibly raise the pH of endocytic vesicles in cultured mouse fibroblasts. J. Cell Biol. 95, 676–681.

McKenna, A., et al., 2010. The Genome Analysis Toolkit: a MapReduce framework for analyzing next-generation DNA sequencing data. Genome Res. 20, 1297–1303.

Meusser, B., et al., 2005. ERAD: the long road to destruction. Nat. Cell Biol. 7, 766–772.

Miao, Y., et al., 2015. A TRP channel senses lysosome neutralization by pathogens to trigger their expulsion. Cell 161, 1306–1319.

Miyazaki, E., et al., 2001. NHE6 protein possesses a signal peptide destined for endoplasmic reticulum membrane and localizes in secretory organelles of the cell. J. Biol. Chem. 276, 49221–49227.

Mobius, W., et al., 2003. Recycling compartments and the internal vesicles of multivesicular bodies harbor most of the cholesterol found in the endocytic pathway. Traffic 4, 222–231.

Nakamura, N., et al., 2005. Four Na^+/H^+ exchanger isoforms are distributed to Golgi and post-Golgi compartments and are involved in organelle pH regulation. J. Biol. Chem. 280, 1561–1572.

Nygaard, E.B., et al., 2011. Structural modeling and electron paramagnetic resonance spectroscopy of the human Na^+/H^+ exchanger isoform 1, NHE1. J. Biol. Chem. 286, 634–648.

Ohgaki, R., et al., 2010. The Na^+/H^+ exchanger NHE6 in the endosomal recycling system is involved in the development of apical bile canalicular surface domains in HepG2 cells. Mol. Biol. Cell 21, 1293–1304.

Ouyang, Q., et al., 2013. Christianson syndrome protein NHE6 modulates TrkB endosomal signaling required for neuronal circuit development. Neuron 80, 97–112.

Park, M., et al., 2006. Plasticity-induced growth of dendritic spines by exocytic trafficking from recycling endosomes. Neuron 52, 817–830.

Pescosolido, M.F., et al., 2014. Genetic and phenotypic diversity of NHE6 mutations in Christianson syndrome. Ann. Neurol. 76, 581–593.

Presley, J.F., et al., 1997. Bafilomycin A1 treatment retards transferrin receptor recycling more than bulk membrane recycling. J. Biol. Chem. 272, 13929–13936.

Raiborg, C., Stenmark, H., 2009. The ESCRT machinery in endosomal sorting of ubiquitylated membrane proteins. Nature 458, 445–452.

Rajendran, L., et al., 2014. Emerging roles of extracellular vesicles in the nervous system. J. Neurosci. 34, 15482–15489.

Roxrud, I., et al., 2009. Dual degradation mechanisms ensure disposal of NHE6 mutant protein associated with neurological disease. Exp. Cell Res. 315, 3014–3027.

Ruddock, L.W., Molinari, M., 2006. N-glycan processing in ER quality control. J. Cell Sci. 119, 4373–4380.

Scheel, O., et al., 2005. Voltage-dependent electrogenic chloride/proton exchange by endosomal CLC proteins. Nature 436, 424–427.

Schwede, M., et al., 2013. Genes for endosomal NHE6 and NHE9 are misregulated in autism brains. Mol. Psychiatry 19, 277–279.

Seglen, P.O., et al., 1979. Inhibition of the lysosomal pathway of protein degradation in isolated rat hepatocytes by ammonia, methylamine, chloroquine and leupeptin. Eur. J. Biochem. 95, 215–225.

Sikora, J., et al., 2016. X-linked Christianson syndrome: heterozygous female Slc9a6 knockout mice develop mosaic neuropathological changes and related behavioral abnormalities. Dis. Model. Mech. 9, 13–23.

Simons, M., Raposo, G., 2009. Exosomes-vesicular carriers for intercellular communication. Curr. Opin. Cell Biol. 21, 575–581.

Sinajon, P., et al., 2016. The expanding phenotypic spectrum of female SLC9A6 mutation carriers: a case series and review of the literature. Hum. Genet. 135 (8), 841–850.

Stenseth, K., Thyberg, J., 1989. Monensin and chloroquine inhibit transfer to lysosomes of endocytosed macromolecules in cultured mouse peritoneal macrophages. Eur. J. Cell Biol. 49, 326–333.

Stromme, P., et al., 2011. X-linked Angelman-like syndrome caused by Slc9a6 knockout in mice exhibits evidence of endosomal-lysosomal dysfunction. Brain 134, 3369–3383.

Teter, K., et al., 1998. Cellubrevin-targeted fluorescence uncovers heterogeneity in the recycling endosomes. J. Biol. Chem. 273, 19625–19633.

Trajkovic, K., et al., 2008. Ceramide triggers budding of exosome vesicles into multivesicular endosomes. Science 319, 1244–1247.

Vella, L.J., et al., 2016. Focus on Extracellular Vesicles: Exosomes and their Role in Protein trafficking and Biomarker potential in Alzheimer's and Parkinson's Disease. Int. J. Mol. Sci. 17, 173.

Weisz, O.A., 2003. Acidification and protein traffic. Int. Rev. Cytol. 226, 259–319.

Wubbolts, R., et al., 2003. Proteomic and biochemical analyses of human B cell-derived exosomes Potential implications for their function and multivesicular body formation. J. Biol. Chem. 278, 10963–10972.

Xinhan, L., et al., 2011. Na^+/H^+ exchanger isoform 6 (NHE6/SLC9A6) is involved in clathrin-dependent endocytosis of transferrin. Am. J. Physiol Cell Physiol. 301, C1431–C1444.

Xu, H., et al., 2007. Activating mutation in a mucolipin transient receptor potential channel leads to melanocyte loss in varitint-waddler mice. Proc. Natl. Acad. Sci. U. S. A. 104, 18321–18326.

Yamashiro, D.J., et al., 1984. Segregation of transferrin to a mildly acidic (pH 6.5) Para-Golgi compartment in the recycling pathway. Cell 37, 789–800.